Article:

Rahmani Ghourtani, Mostafa orcid.org/0000-0002-7943-9977, Zhao, Junbo, Chu, Yi et al. (4 more authors) (2025) Link-Level Evaluation of Uplink Cell-Free MIMO in 5G NR over Frequency-Selective Channels. IEEE Open Journal of the Communications Society. ISSN: 2644-125X

https://doi.org/10.1109/OJCOMS.2025.3587990

IEEE ComSoc IEEE Communications Society

IEEE Open Journal of the Communications Society

Received XX Month, XXXX; revised XX Month, XXXX; accepted XX Month, XXXX; Date of publication XX Month, XXXX; date of current version 11 January, 2024.

Digital Object Identifier 10.1109/OJCOMS.2024.011100

Link-Level Evaluation of Uplink Cell-Free MIMO in 5G NR over Frequency-Selective Channels

Mostafa Rahmani Ghourtani[1], Junbo Zhao[1], Yi Chu[1], Hamed Ahmadi[1], David Grace[1], Robert G. Maunder[2], Alister Burr[1]

[1]School of Physics, Engineering and Technology, University of York, UK
[2]Department of Electronics and Computer Science, University of Southampton, UK

CORRESPONDING AUTHOR: Mostafa Rahmani Ghourtani (e-mail:rahmani.mostafa@york.ac.uk).

The work presented in this paper was funded by UK Department for Science, Innovation and Technology under projects YO-RAN and DU-Volution.

ABSTRACT Cell-free (CF) MIMO has emerged as a promising next-generation technology, primarily due to its ability to provide uniformly high-quality service to all user equipment (UEs), regardless of their location. While existing research has extensively explored various aspects of CF systems—including scalability, clustering strategies, power control, and precoding designs—there remains a notable gap in the literature concerning the physical-layer performance of 5G New Radio (NR) within CF architectures. This paper addresses this gap by focusing on the Physical Uplink Shared Channel (PUSCH) transmission over frequency-selective channels. We develop a comprehensive, 3GPP-compliant link-level simulator to evaluate the performance of CF MIMO under realistic propagation conditions. First, we generate results for selected modulation and coding schemes (MCSs) to confirm the simulator's alignment with expected performance. Then, the effects of key physical-layer parameters—such as subcarrier spacing (SCS), the number of distributed radio units (RUs), and the number of RU antennas—are evaluated using Block Error Rate (BLER) as the primary performance metric. We also compare the results of the CF-MIMO system with a co-located antenna scenario, serving as the baseline for a traditional MIMO system, and confirm that the CF-MIMO system achieves superior performance due to its spatial diversity advantages. The results also show that employing higher SCS values effectively exploits frequency diversity, particularly when the signal bandwidth exceeds the channel's coherence bandwidth. As expected, increasing the number of RUs significantly improves BLER due to enhanced spatial diversity and reduced UE-RU path loss. We further examine the impact of practical channel estimation by evaluating four different DMRS configurations, confirming that Type 1 with length 2 provides superior performance under the tested conditions. Finally, we investigate the effect of carrier frequency, showing that higher frequencies lead to increased path loss and degraded performance. The findings offer valuable insights into spatial, frequency, and estimation-related interactions in CF 5G NR, while guiding MCS selection for target BLER-SNR levels and enabling PHY abstraction for higher-layer simulations.

INDEX TERMS Block error rate, Cell-free system, Link level simulation, Physical uplink shared channel, 5G New Radio.

I. Introduction

With next-generation demands for higher data rates, broader coverage, and enhanced user experience, cell-free multiple-input multiple-output (CF-MIMO) technology is emerging as a key solution [1]. Unlike traditional cellular networks, CF-MIMO effectively removes cell boundaries, creating a cooperative network of access points (APs) or radio units (RUs) that collectively serve all user equipment (UE). This design improves coverage and throughput, particularly at network edges, by leveraging macro-diversity. In CF-MIMO, distributed APs connect to a central processing unit (CPU) through a fronthaul network for synchronized transmission and reception, enhancing signal quality (SNR and SINR) network-wide [2], [3]. Alongside CF-MIMO, 5G New Radio (NR) technology, developed by the Third Generation Partnership Project (3GPP), has progressed rapidly [4].

CF-MIMO architectures have garnered significant research interest over the past decade, establishing foundational elements such as uplink and downlink operation, pilot assignment, pilot decontamination, channel estimation, and power control algorithms [5]–[8]. However, most studies have assumed single-carrier transmission, which is appropriate for block-wise frequency-flat, time-invariant fading channels, where the channel fading remains constant across the entire time-frequency resource grid. While this assumption simplifies analysis and can provide accurate approximations when RBs fit within the channel's coherence bandwidth and time, real-world wireless channels are inherently frequency-selective and time-varying.

Research on CF-MIMO systems that accounts for bandwidth and frequency-selective channels is still sparse. Only few studies address performance in frequency-selective channels, with channel aging and phase noise examined in limited works. Zheng et al. [9] provided closed-form uplink and downlink rate expressions that consider channel aging, spatial correlation, and pilot contamination, showing that CF-MIMO is more resilient to channel aging than small cell systems. In [10], Jiang et al. investigate how channel aging and phase noise affect the performance of zero-forcing precoding in CF-MIMO systems. They argue that the exchange of channel state information (CSI) and precoded data over a fronthaul network incurs considerable delay, which necessitates the use of delay-aware techniques like channel prediction to mitigate its impact.

In [11], the authors investigate the effects of frequency-selective fading channels on the design and performance of CF-MIMO orthogonal frquency-division multiplexing (CF-MIMO-OFDM) networks, providing a comprehensive characterization of time and frequency selectivity as well as inter-carrier interference. Furthermore, an innovative opportunistic AP selection scheme aimed at enhancing time-frequency resource utilization in a CF-MIMO-OFDM system was introduced in [12]. The approach assigns subcarriers orthogonally to users, ensuring only one user per subcarrier, and serves each user only through nearby APs while deactivating distant APs to reduce power wastage on high-loss channels. This selective activation reduces the number of active APs per subcarrier, enabling feasible downlink pilot use and coherent detection.

In [13] the performance of CF-MIMO-OFDM systems in high-speed train communications is analyzed, considering fully centralized and local minimum mean square error (MMSE) combining. The study derives closed-form expressions for uplink spectral efficiency, accounting for local maximum ratio combining, large-scale fading decoding cooperation, and the impact of Doppler frequency offset on system performance. Building on these insights, our study examines practical channel estimation effects and compares them with ideal channel estimation to assess realistic performance bounds in CF architectures. In [14] OFDM-based multi-carrier transmission approach for CF-MIMO systems over frequency-selective fading channels is presented and analyzed. The study proposes frequency-domain conjugate beamforming, pilot assignment, and user-specific resource allocation strategies to enhance system performance. Additionally, the method of superimposed pilots for channel estimation in CF-MIMO-OFDM systems has been investigated and documented in [15].

While most research on CF-MIMO systems has focused on evaluating spectral efficiency and energy efficiency, other vital performance metrics, such as outage probability (OP) and error performance analysis, have been relatively underexplored. These metrics are crucial for assessing system reliability in real-world scenarios. Determining a closed-form expression for OP is particularly challenging due to the complex nature of CF-MIMO systems [16]. In [17], a closed-form expression for the OP in full-duplex CF-MIMO systems is derived and verified using analytical approaches and simulations, including an analysis of asymptotic performance. The study considers the effects of imperfect CSI and user mobility, allowing multiple user equipments (UEs) to operate on shared spectrum resources.

To the best of the authors' knowledge, no prior research has examined the implementation CF-MIMO systems based on 5G NR with Physical Uplink Shared Channel (PUSCH) fully aligned to 3GPP standards. While CF-MIMO systems have been widely studied in theoretical contexts, existing works often rely on simplified or custom waveform and protocol assumptions, diverging from practical 3GPP-compliant architectures. This gap underscores the significance of this study, which aims to bridge theory and practice by leveraging the standardized 5G NR framework. Such alignment not only ensures interoperability with existing networks but also provides a realistic foundation for evaluating CF-MIMO systems in real-world deployment scenarios.

This study contributes to addressing this gap by providing simulation results grounded in the 5G NR air interface. A focal point of this work is the analysis of Block Error Rate (BLER), a key metric for assessing link quality in modern communication systems. BLER is especially significant in 5G networks, where adaptive modulation, coding, and resource allocation strategies depend on maintaining target BLER thresholds as defined in 3GPP TS 23.501. These thresholds are tailored to meet the stringent quality of service (QoS) requirements of diverse applications, ranging from ultra-reliable low-latency communication to enhanced mobile broadband. While this work focuses on BLER as the main metric, as it is the key link-level indicator of PHY-layer reliability, future work will extend the simulator framework to support additional higher-layer metrics such as throughput, latency, fairness, and QoS, which

TABLE 1. **Comparison of This Work with Existing Studies in Cell-Free MIMO**

Feature	**This Work**	[2]	[3]	[11]	[13]	[14]	[15]	[18]
Simulation Level	**Link-level**	System-level	System-level	System-level	System-level	System-level	System-level	✗ Testbed
Deployment Type	**Fixed**	Random	Random	Random	Random	Random	Random	Fixed
Standard Compliance (5G NR)	✔	✗	✗	✗	✗	✗	✗	✔
Performance Metric	**BLER**	Throughput	Spectral efficiency	User rate	spectral efficiency	Sum rate	Sum rate; BER	Throughput
CDF-Based Evaluation	✗	✔	✔	✔	✔	✔	✔	✗
Massive MIMO	✗ (8 RU)	✔	✔	✔	✔	✔	✔	✗
OFDM waveforms	✔	✗	✗	✔	✔	✔	✔	✔
Channel Model (Fading model)	**Freqency selective**	Block fading	Block fading	Block fading	Block fading	Freqency selective	Freqency selective	Practical, Real
Channel Estimation with DMRS	✔	✗	✗	✗	✗	✗	✗	✔
MCS analysis	✔	✗	✗	✗	✗	✗	✗	✔
Uplink (PUSCH) Focus	✔	✗	✗	✗	✗	✗	✗	✔

require system-level and cross-layer modeling. Unlike prior works that primarily evaluate system-level metrics—such as spectral efficiency or energy efficiency—over a wide range of random network configurations and present results in terms of cumulative distribution functions (CDFs), our approach takes a different direction. In this study, we focus on a fixed, representative deployment scenario. By fixing the deployment, we ensure a meaningful evaluation of BLER performance, which inherently requires a stable configuration to yield interpretable and reproducible results. This link-level perspective offers complementary insights to existing system-level analyses and supports the development of accurate PHY abstraction models for CF MIMO in 5G NR. In line with this direction, the authors' research group has recently initiated practical investigations into CF-MIMO systems. In [18], testbed results are presented for an intelligent O-RAN-based cell-free MIMO network, demonstrating early-stage hardware feasibility. In [19], detailed link-level simulations are performed for wiretap channels under various frequency-selective fading scenarios and noise conditions, utilizing tapped delay line channel models as defined in 3GPP TR 38.901. These efforts collectively reflect a broader initiative to evaluate and validate CF-MIMO systems under both realistic physical conditions and standardized protocol environments.

Despite its importance, the exploration of BLER performance in CF-MIMO-OFDM systems remains limited in existing literature, with most studies focusing on traditional setups that overlook the distributed nature and unique architectural characteristics of CF-MIMO. By analyzing BLER curves within the CF-MIMO-OFDM framework, this paper provides critical insights into the interaction of distributed MIMO architectures with 5G NR air interfaces, aiming to establish a foundational understanding of how CF-MIMO can deliver reliable and efficient communication in real-world scenarios. The findings highlight its potential to meet the diverse and demanding requirements of next-generation wireless networks. Notably, the comparative analysis reveals that different UEs within the same CF-MIMO system exhibit varying slopes in their BLER versus SNR performance, despite sharing the same frequency bandwidth, being served by the same RUs, and affected by the same channel conditions. This variation underscores the complexity and dynamic behavior of CF-MIMO systems, emphasizing the need for further investigation. Understanding these differences could offer valuable insights into optimizing QoS distribution and ensuring equitable service reliability across all UEs in the network. The main contributions of this study are summarized as follows:

1. We design a link-level simulator tailored for an uplink CF-MIMO system, incorporating all the PUSCH processing procedures as defined by the 3GPP standards for 5G NR. BLER is employed as a primary metric to evaluate and compare system performance across different setups. This approach provides meaningful insights into reliability under various configurations.
2. We examine the impact of crucial parameters, including different sub-carrier spacings, varying numbers of RUs, different numbers of RU antennas, and different modulation schemes: quadrature phase shift keying (QPSK), 16 quadrature amplitude modulation (16-QAM), 64-QAM, 256-QAM.

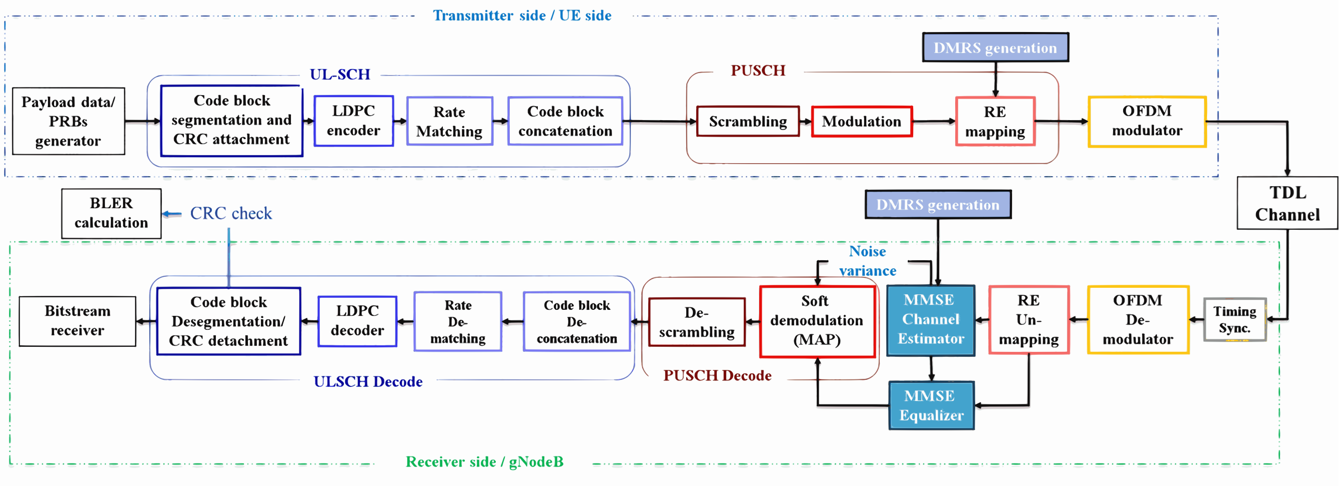

FIGURE 1. **Transmitter and receiver chain of the 5G NR PUSCH channel.**

3. We investigate the interplay between frequency-selective channels and the CF architecture, demonstrating how the combination of spatial and frequency diversity enhances resource exploitation and ensures consistent performance across users and channel conditions. This focus provides critical insights into the potential of CF-MIMO systems to address fading and improve reliability in next-generation wireless networks.
4. We investigate the effects of practical channel estimation by comparing it with ideal (perfect) channel estimation, demonstrating the performance implications of realistic channel estimation in a CF-MIMO system.
5. We compare the performance of the CF-MIMO system with a co-located antenna configuration representing a traditional MIMO baseline. Specifically, we assume that a single centralised base station is equipped with the same total number of antennas as the combined antennas deployed across all RUs in the distributed CF-MIMO setup. This allows for a fair comparison and confirms the performance advantages of the CF-MIMO system, primarily due to its enhanced spatial diversity.

The key differences between our work and previous studies in the literature are summarized in Table 1, highlighting aspects such as deployment configuration, simulation level, performance metrics, and compliance with 5G NR standards. Unlike prior system-level studies, our work offers a detailed link-level evaluation that captures realistic physical-layer effects, providing complementary insights often overlooked in system-level analyses.

The rest of the paper is organized as follows: In Section II, we first present a brief overview of 5G NR PUSCH, followed by the proposed structure of a 5G-based link-level simulator for CF-MIMO systems. Section III describes the system and channel models, and also the UL training and payload data transmission phase. The BLER analysis of the CF-MIMO system is studied in Section IV by considering all the performance metrics. Finally, conclusions are drawn, and future work is discussed in Section VI.

Notation: We will adopt the following notations in the rest of the paper. The superscripts $()^*$, $()^T$ and $()^H$ represents the complex conjugate, transpose, and conjugate-transpose, respectively. An uppercase boldface letter stands for a matrix or a vector with the elements in the frequency domain, while a lowercase boldface letter represents a vector in the time domain.

II. PRELIMINARIES for 5G-based Link-Level Simulator

This section is organized into three subsections, each addressing a key aspect of the link level simulator. Subsection A outlines the core principles of 5G NR, emphasizing the PUSCH processing. Subsection B discusses the alignment of CF-MIMO systems with the O-RAN architecture, and subsection C details the simulator's workflow, from UE payload transmission through a modeled channel to centralized DU processing, including channel estimation, equalization, decoding, and error calculation.

A. 5G New Radio

Selecting an appropriate radio waveform is crucial for mobile access technologies, as it significantly impacts system performance [20]. In 5G NR, OFDM with Cyclic Prefix (CP-OFDM) is adopted for both downlink and uplink transmissions, as recommended by 3GPP. This choice is due to CP-OFDM's low implementation complexity, cost-effectiveness for wide bandwidths, and MIMO systems.

Fig.1 illustrates the physical layer processing of the 5G NR PUSCH including transmitter and receiver chains [21]. The PUSCH processing at the transmitter side consists of several steps: first, a Cyclic Redundancy Check (CRC) is added to the payload for error detection. The payload is then segmented into code blocks, which are individually encoded using Low-Density Parity-Check (LDPC) coding, tailored to the payload size. Following LDPC encoding, rate matching

TABLE 2. **Main Acronym Used in Paper**

Acronym	definition
3GPP	Third-generation partnership project
5G	Fifth generation
AP	Access point
AWGN	Additive white Gaussian noise
BLER	Block error rate
BS	Base station
CDF	Cumulative distribution function
CE	Channel estimation
CF-MIMO	Cell-free MIMO
CP	Cyclic prefix
CRC	Cyclic redundancy check
CSI	Channel state information
CU	Central unit
DMRS	Demodulation reference signal
DU	Distributed unit
HPC	High performance computing
IQ	In-phase and quadrature
LDPC	Low-density parity-check
LLR	Log-likelihood ratio
MCS	Modulation and coding scheme
MIMO	Multiple-input multiple-output
MMSE	Minimum mean square error
NLOS	Non-line-of-sight
NR	New radio
OCC	Orthogonal cover code
OFDM	Orthogonal frequency-division multiplexing
OP	Outage probability
O-RAN	Open radio access network
PHY	Physical layer
PRB	Physical resource block
PUSCH	Physical uplink shared channel
QAM	quadrature amplitude modulation
Qos	Quality of service
QPSK	quadrature phase shift keying
RU	Radio unit
SCS	Subcarrier spacing
SINR	Signal-to-interference-plus-noise ratio
SNR	Signal-to-noise ratio
TDL	Tapped delay line
TX-SNR	Transmit SNR
UE	User equipment
UL-SCH	Uplink shared channel
ZF	Zero forcing

is performed to adjust the coding rate to match the channel capacity. The resulting code blocks are concatenated into a single codeword, which is subsequently scrambled and modulated using the QPSK, 16-QAM, 64-QAM, or 256-QAM modulation, depending on the PUSCH requirements. The modulated symbols are then layer-mapped according to the available antenna ports, followed by precoding for transmission. Finally, the symbols are mapped to the resource grid, ensuring efficient allocation of frequency and time resources for OFDM signal generation, ready for transmission over the channel.

The receiver processing chain in 5G NR starts with the OFDM demodulator, which converts the received time-domain signal into the frequency domain and removes the cyclic prefix. The demodulated signal is then subjected to layer and RE demapping to separate signals from multiple layers and align them with their corresponding Resource Elements (REs). MMSE channel estimation is performed using Demodulation Reference Signal (DMRS) to derive CSI, followed by MMSE equalization to mitigate channel fading and interference.

The equalized data undergoes soft demodulation, converting the symbols into Log-Likelihood Ratios, which are then descrambled to restore the original encoded sequence. Rate dematching reverses the rate matching process, restoring the encoded sequence length, which is then passed to the LDPC decoder for error correction. The decoded data is desegmented, and the CRC is detached and checked for errors. Finally, the error-checked data is passed to the bitstream receiver, and the BLER calculation evaluates the overall system performance. This structured process ensures reliable recovery of transmitted data in complex wireless environments.

B. Cell-Free System in O-RAN Networks

CF-MIMO systems require fine-grained processing flexibility, such as task allocation between APs and CPUs, and this aligns naturally with the Open Radio Access Networks (O-RAN) disaggregation concept. O-RAN, standardizes RAN functionality through its architecture, which separates the radio access network into the central unit (CU), distributed unit (DU), and radio unit (RU). Within this framework, the CPU in CF-MIMO systems corresponds to the DU, and APs correspond to RUs, enabling better alignment of CF-MIMO system with industry standards. The O-RAN 7-2x functional split divides the physical layer processing between DUs and RUs, balancing simplicity in RUs with fronthaul efficiency. This architectural alignment facilitates practical CF implementations, leveraging O-RAN's standardized framework to advance CF-MIMO systems in real-world deployments [22].

C. Cell-Free MIMO Link-Level Simulator Architecture

Figures 2 and 3 illustrate the architecture of the proposed link-level simulator for evaluating CF MIMO systems in uplink. This simulator is designed to be fully compliant with the 5G NR physical layer and leverages the MATLAB 5G Toolbox. However, it introduces several significant extensions to support distributed reception, centralized decoding, and spatial cooperation RUs.

1) System Overview and Transmission Chain (Figure 2)

Figure 2 presents the end-to-end simulation architecture, structured into three main stages: the UE side, the wireless channel, and the receiver side (RU + DU). On the UE side,

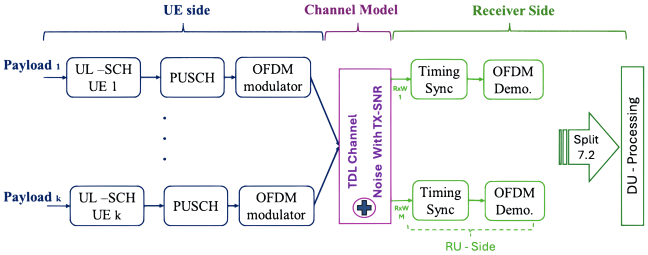

FIGURE 2. Block diagram of link-level simulator for Cell-free system.

K single-antenna UEs transmit independent payloads using a standardized 5G NR uplink chain, which includes: (1) UL-SCH encoding,(2) PUSCH channel coding, and (3) CP-OFDM modulation. These blocks are directly reused from MATLAB's 5G Toolbox with standard parameter settings, ensuring full 3GPP alignment. All UEs transmit concurrently over the same time-frequency resources, naturally introducing multi-user interference—a fundamental aspect of CF-MIMO systems. The wireless propagation environment is modeled using a Tapped Delay Line (TDL) channel with additive white Gaussian noise (AWGN). The transmit signal-to-noise ratio (TX-SNR) is adjustable to simulate various channel conditions, ensuring realism in multi-path fading, delay spread, and interference.

2) RU-Side Reception and Signal Forwarding

Each of the M distributed RUs receives a composite signal from all UEs, denoted RxW_1 through RxW_M. Each RU performs local baseband processing, including: Timing synchronization, CP removal, and OFDM demodulation. These modules are reused from the 5G Toolbox but are adapted to ensure consistency in signal alignment and normalization across multiple distributed receivers. Importantly, this processing is performed independently and in parallel at each RU, without knowledge of other RUs' signals.

After OFDM demodulation, frequency-domain data streams are forwarded to the DU for centralized baseband processing. This design follows functional split 7.2, where high-PHY operations—such as channel estimation, equalization, and decoding—are offloaded to the DU, preserving lightweight operation at the RUs and enabling scalable centralized coordination.

3) DU Processing and Centralized Decoding (Figure 3)

Figure 3 details the key innovation of the simulator: the DU-side centralized processing pipeline, where the simulator departs from the conventional PUSCH chain and enables cell-free operation.

Channel Estimation:

The DU performs centralized pilot-based channel estimation to construct a global channel matrix $\hat{H} \in \mathbb{C}^{M\times K}$, representing the channel between each UE and RU. This block is adapted from standard toolbox routines to aggregate pilot observations across all RUs.

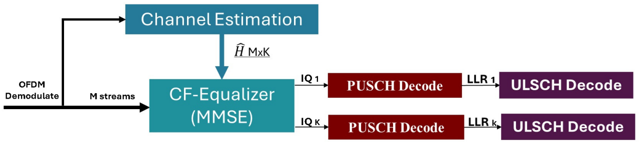

FIGURE 3. DU Processing Stages in Cell-Free Link-Level Simulator

CF-MMSE Equalization:

A cell-free MMSE equalizer processes the M demodulated RU streams jointly using $\hat{H}$. Unlike traditional equalizers, this block performs global interference suppression and soft symbol recovery, outputting per-user streams $\mathrm{IQ}_1, \ldots, \mathrm{IQ}_K$. This centralized equalization is critical to leveraging the spatial diversity of the distributed system and constitutes a core novelty of the simulator.

PUSCH Soft Demodulation:

The IQ streams are demodulated using Toolbox-based modules (e.g., QAM demapping, layer separation, descrambling). These blocks are reused with minimal adaptation but are restructured to support parallel stream processing and downstream decoding.

UL-SCH (LDPC) Decoding:

Soft bits (LLRs) are passed to LDPC decoders to recover the transmitted information. While the decoders themselves are standard, the simulator manages LLR scaling and synchronization carefully to maintain decoding accuracy across multiple users and streams.

4) Key Differentiators from the Conventional PUSCH Chain

The simulator retains standard 5G components where appropriate but introduces substantial innovations to enable CF-MIMO simulation. Table 3 summarizes the key differences: Together, Figures 2 and 3 define a full-stack link-level simulator capable of modeling and evaluating CF-MIMO systems under realistic 5G NR conditions. By combining reused 3GPP-compliant components with custom adaptations for distributed reception and centralized decoding, the simulator provides a scalable and modular platform for studying cell-free architectures beyond what is possible with conventional link-level tools. This architecture supports flexible configuration of user density, RU deployment, channel conditions, and processing algorithms—making it well-suited for benchmarking physical layer trade-offs and guiding the design of future CF-MIMO networks.

III. System Model

The section is organized into five subsections that collectively explain the components and processes of the uplink data transmission and channel estimation in 5G NR-based systems. Subsection A introduces the flexible time-frequency organization of 5G NR. Subsequently, Subsection B details the channel, modeled as a tapped delay line to account for multipath propagation effects. Following this, Subsection C explains the OFDM-based transmission process. Furthermore, Subsection D focuses on the use of DMRS for channel

TABLE 3. Comparison between Conventional PUSCH and CF-MIMO Simulator

Component	Conventional PUSCH Chain	CF-MIMO Simulator
Channel Estimation	Local, per-RU	Joint, across all RUs
Equalization	Per-link MMSE or ZF	Centralized CF-MMSE equalizer
Receiver Inputs	Single RU	M distributed RUs
UE-RU Association	Simple one-to-one link	Fully cooperative, all RUs serve all UEs
Interference Handling	-	Global interference suppression
Toolbox Usage	Unmodified standard chain	Selective reuse + structural modifications

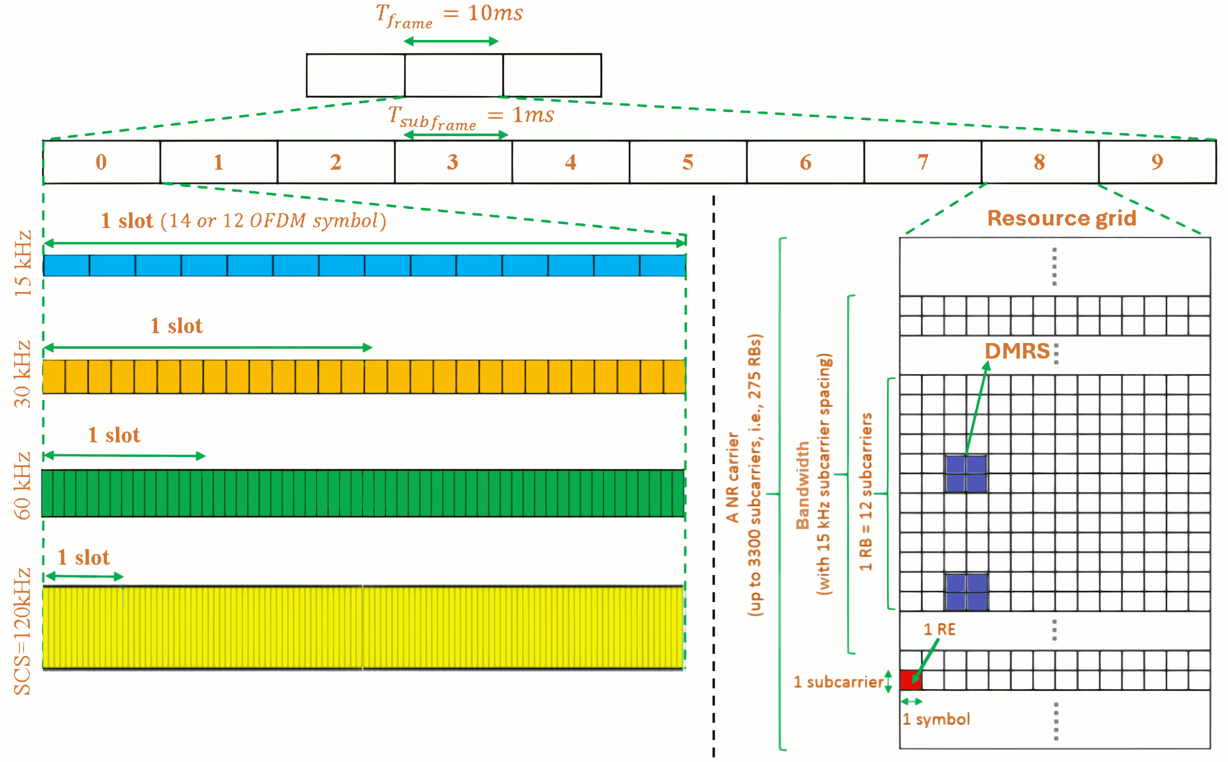

FIGURE 4. Illustration of 5G NR transmission structure in time and frequency domain by considering four different subcarrier spacing [4].

estimation. Finally, Subsection E describes the Uplink data transmission.

A. Frame and Pilot Structure

In 5G NR, uplink (and downlink) data transmission is organized into 10 ms frames, each divided into 10 subframes of 1 ms. Each subframe consists of a variable number of slots, depending on the selected subcarrier spacing Δf, allowing flexibility. In the normal case, a slot contains 14 OFDM symbols, each with a cyclic prefix, whereas in the extended cyclic prefix (CP) option, a slot contains 12 OFDM symbols with a longer cyclic prefix. The smallest unit, a RE, is a subcarrier within the passband, and 12 consecutive REs in the same symbol form a Physical Resource Block (PRB). This flexible frame structure, as shown in Fig. 4, enables 5G NR to meet diverse requirements for cell size, latency, and interference resilience [21].

The 5G NR standard defines two types of reference signals associated with the transmission of the PUSCH channel. The DMRS is a user-specific reference signal with high frequency density, dedicated for frequency-selective channel estimation [23, Sec. 6.4.1.1]. It occupies specific OFDM symbols within each slot, with the number of OFDM symbols containing DMRS varying between 1 and 4 depending on the configuration. For rapidly changing channels, a higher density of DMRS symbols in time helps obtain more accurate channel estimates within the coherence time. In the frequency domain, DMRS symbols are mapped across the entire set of PRBs allocated to the PUSCH, and the spacing between DMRS REs assigned to the same RU can be set to 2 or 3 RE. In this work, we consider only DMRS for channel estimation.

B. Channel Model

Unlike previous research that assumes a flat-fading channel, this study adopts a more comprehensive approach by considering a channel model that is both time-selective and frequency-selective, making it suitable for analyzing broadband scenarios and capturing the dynamic behavior of real-world wireless channels. In practice, the channel fading

TABLE 4. Definition of Main Mathematical symbols

Symbols	Meanings
M, K	Number of RUs and UEs
β_{mk}	Large-scale fading coefficient between the k-th UE and the m-th RU
$\mathbf{h}$	Tapped delay line vector in the time domain
L_{mk}	Number of taps for the link between the k-th UE and the m-th RU
$\mathbf{g}_{mk}$	Channel coefficient vector between the k-th UE and the m-th RU in the time domain
$\mathbf{X}_k$	OFDM symbol vector transmitted by the k-th UE
$X_{k,n}$	OFDM symbol on the n-th subscarrier transmitted by the k-th UE
$\mathbf{x}_k$	Data sequence vector transmitted by the k-th UE in the time domain
$Y_{m,n}$	Received symbol on the n-th subscarrier at the m-th RU
$\mathbf{G}_{mk}$	Channel frequency response vector between the k-th UE and the m-th RU
$G_{mk,n}$	Channel frequency response on the n-th subscarrier between the k-th UE and the m-th RU
$Z_{m,n}$	Noise on the n-th subscarrier at the m-th RU in the frequency domain
$\mathbf{Y}_m^p$	Received DMRS signal at the m-th RU
$\mathbf{P}_k$	DMRS symbols used by the k-th UE in a vector
$\mathbf{Z}_m^p$	Vector of noise at the m-th RU in the pilot (DMRS) positions
$\hat{\mathbf{G}}_{mk}$	Channel frequency response estimates for the k-th UE and m-th RU
S_k	Modulated symbol transmitted by the k-th UE on the n-th subcarrier
σ_Z^2, σ_S^2	Variance of the noise and modulated symbol in frequency domain
p_k	Transmitted power for the modulated symbol
$\mathbf{W}_{k,n}$	Weight vector for detecting the symbol transmitted by the k-th UE on the n-th subcarrier
N_{SG}, N_{fft}	Number of the resource blocks and FFT points

is frequency selective, and can be modelled as a tapped delay line $\mathbf{h} = [h_0, \ldots, h_{L_{mk}-1}]^{\mathrm{T}}$, where L_{mk} is the number of multipath channel taps for the link between the k-th UE and the m-th RU. The normalized delay and corresponding power for the tapped delay line model is provided by 3GPP [24, Sec. 7.7.2]. The channel coefficient between the k-th UE and the m-th RU is then given by

$$\mathbf{g}_{mk} = [g_{mk,0}, \ldots, g_{mk,L_{mk}-1}]^{\mathrm{T}} = \sqrt{\beta_{mk}}\mathbf{h} \tag{1}$$

where β_{mk} is the large-scale fading coefficient, as detailed in Section B.

C. Signal Model

We define the N-point transmission block for a single OFDM symbol sent by the k-th UE as $\mathbf{X}_k = [X_{k,0}, \ldots, X_{k,N-1}]^{\mathrm{T}}$. Through the OFDM modulation, the time domain sequence is given by $\mathbf{x}_k = [x_{k,0}, \ldots, x_{k,N-1}]^{\mathrm{T}}$ in which the i-th element is $x_{k,i} = \frac{1}{N}\sum_{n=0}^{N-1} X_{k,n} e^{2\pi j \frac{ni}{N}}$, where $i = 0, 1, \ldots, N-1$ and j denotes the imaginary unit. The sequence can also be written in matrix form as

$$\mathbf{x}_k = \frac{1}{N}\mathbf{F}_N^* \mathbf{X}_k \tag{2}$$

where $\mathbf{F}_N$ is the $N \times N$ discrete Fourier transform (DFT) matrix. Also, the CP is added to avoid inter-symbol interference (ISI), leading to the sequences $\mathbf{x}_k^{\mathrm{cp}}$. Through the multipath fading channel, the received signal at the m-th RU is given by $\mathbf{y}_m^{\mathrm{cp}} = \sum_{k=1}^{K} \mathbf{x}_k^{\mathrm{cp}} * \mathbf{g}_{mk} + \mathbf{z}_m^{\mathrm{cp}}$, where $*$ denotes the linear convolution and $\mathbf{z}_m^{\mathrm{cp}}$ is the complex additive white Gaussian noise (AWGN) with the variance σ_z^2. Before doing the OFDM demodulation, the received signal should cut the residual tails and remove the CP in order to keep the same length as the OFDM modulated signals. This process can be expressed by [14]

$$\mathbf{y}_m = \sum_{k=1}^{K} \mathbf{g}_{mk}^N \otimes \mathbf{x}_k + \mathbf{z}_m \tag{3}$$

where $\otimes$ denotes the cyclic convolution, $\mathbf{z}_m$ is the part of the noise with size N, and $\mathbf{g}_{mk}^N$ is an N-point channel impulse response formed by padding zeros for $\mathbf{g}_{mk}$. The OFDM demodulated signal is given by

$$\begin{aligned} \mathbf{Y}_m = \mathbf{F}_N \mathbf{y}_m &= \sum_{k=1}^{K} \mathbf{F}_N(\mathbf{g}_{mk}^N \otimes \mathbf{x}_k) + \mathbf{F}_N \mathbf{z}_m \\ &= \sum_{k=1}^{K} \mathbf{G}_{mk} \odot \mathbf{X}_k + \mathbf{Z}_m \end{aligned} \tag{4}$$

where $\odot$ represents the Hadamard product, $\mathbf{G}_{mk} \in \mathbb{C}^{N\times 1}$ denotes the frequency response of $\mathbf{g}_{mk}^N$, and $\mathbf{Z}_m$ is the OFDM demodulation of $\mathbf{z}_m$ which has the variance σ_Z^2. Note that the variance of each element in the frequency domain differs from that in the time domain. The equation (4) demonstrates that the data transmission through a frequency-selective channel can be transformed into traversing a set of independent flat-fading subcarriers by adopting an OFDM system. It is worth mentioning that, here, we assume that the length of the channel's tapped delay line is shorter than the length of the cyclic prefix. The uplink transmission on the n-th subcarrier received at the m-th RU is then expressed as

$$Y_{m,n} = \sum_{k=1}^{K} G_{mk,n} X_{k,n} + Z_{m,n} \tag{5}$$

where $G_{mk,n}$, $X_{k,n}$ and $Z_{m,n}$ denote the n-th subcarrier, transmitted signal and noise in a single OFDM symbol in the frequency domain, respectively. To recover the data symbol, the uplink channel should be estimated for each sub-carrier.

D. Pilot Transmission and Channel Estimation

As mentioned earlier, the DMRS associated with the UL PUSCH transmission enables coherent demodulation of user data in the uplink. In 5G NR, four different categories of DMRS configurations are defined based on type (Type 1 and Type 2) and length (length 1 and length 2). In all our results, we consider Type 2 and length 2, where DMRS symbols are inserted at the 3rd and 4th OFDM symbols, as shown in Fig. 4. Additionally, in Section IV.F, we compare the performance of all four DMRS configurations to highlight the impact of different DMRS types and lengths on system performance.

The sequence that generates the DMRS symbols is $r(n)$, is defined as follows [25]

$$r(n) = \frac{1}{\sqrt{2}}\left(1 - 2\cdot c(2n)\right) + j\cdot\frac{1}{\sqrt{2}}\left(1 - 2\cdot c(2n+1)\right) \quad (6)$$

This is evidently a QPSK modulation scheme, where each symbol is mapped to one of the four constellation points $\left(\pm\frac{1}{\sqrt{2}} \pm j\frac{1}{\sqrt{2}}\right)$ based on a pseudo-random binary sequence $c(n)$. The pseudo-random sequence $c(n)$ is defined in [26, clause 5.2.1].

In a multi-user scenario, DMRS leverages a combination of frequency and code orthogonality to support efficient channel estimation. Code orthogonality is achieved through the use of Orthogonal Cover Codes (OCCs), which employ Walsh sequences to distribute the pilot signal across neighboring time and frequency REs. This approach is referred to as CDM-Multiplexed DM-RS in the 5G NR standards [27].

We assume that DMRS for the k-th UE is represented by a vector $\mathbf{P}_k \in \mathbb{C}^{N_p \times 1}$, where each DMRS vector is orthogonal to the others. The received DMRS at the m^{th} RU are then given by

$$\mathbf{Y}^{\mathrm{p}}_m = \sum_{k=1}^{K} \mathrm{diag}(\mathbf{P}_k)\mathbf{I}_{\mathrm{p}}\mathbf{G}_{mk} + \mathbf{Z}^{\mathrm{p}}_m \quad (7)$$

where $\mathrm{diag}(\mathbf{P}_{\mathrm{k}})$ denotes a diagonal matrix with the vector $\mathbf{P}_k$ placed on its diagonal (size $N_{\mathrm{p}} \times N_{\mathrm{p}}$). $\mathbf{I}_{\mathrm{p}}$ is an $N_{\mathrm{p}} \times N$ pilot indicator matrix in which the i-th row contains one at the position corresponding to the RE where the i-th pilot occurs, zero elsewhere. $\mathbf{Z}^{\mathrm{p}}_m$ represents the vector of noise in the pilot positions.

The least squares channel estimates in DMRS positions are calculated by

$$\begin{aligned}\hat{\mathbf{G}}_{mk} &= \left[\mathrm{diag}(\mathbf{P}_k)\right]^{-1} \overbrace{\left(\sum_{k'=1}^{K} \mathrm{diag}(\mathbf{P}_{k'})\mathbf{I}_{\mathrm{p}}\mathbf{G}_{mk'} + \mathbf{Z}^{\mathrm{p}}_m\right)}^{\mathbf{Y}^{\mathrm{p}}_m} \\ &= \mathbf{I}_{\mathrm{p}}\mathbf{G}_{mk} + \sum_{k'\neq k}^{K} \boldsymbol{\Theta}_{kk'}\mathbf{I}_{\mathrm{p}}\mathbf{G}_{mk'} + \boldsymbol{\zeta}_m. \end{aligned} \quad (8)$$

where $\boldsymbol{\Theta}_{kk'} = [\mathrm{diag}(\mathbf{P}_k)]^{-1}\mathrm{diag}(\mathbf{P}_{k'})$ is a diagonal matrix and the weighted noise denotes $\boldsymbol{\zeta}_m = [\mathrm{diag}(\mathbf{P}_k)]^{-1}\mathbf{Z}^{\mathrm{p}}_m$.

This limited-length channel estimate can be expanded to all sub-carriers and 14 OFDM symbols within a single resource grid through interpolation. When the DMRS occupies two OFDM symbols (with a DMRS length of two), the same equations (7) and (8) are used to obtain the channel estimates for both OFDM symbols. To estimate the channels for the full resource grid, interpolation is first applied across all subcarriers. Then, using the channel estimates obtained from the two OFDM symbols, interpolation is extended over the time domain to cover all 14 OFDM symbols.

E. Uplink Data Transmission

On the uplink, we suppose the k-th UE transmits the PUSCH modulated symbol $S_{k,n}$, $\sigma_S^2 = \mathbb{E}\{|S_{k,n}|^2\} = 1$, with the power p_k on the n-th subcarrier. Substituting $X_{k,n} = \sqrt{p_k}S_{k,n}$ into (4), the received signal in the n-th RE at the m-th RU is

$$Y_{m,n} = \sqrt{p_k}\sum_{k=1}^{K} G_{mk,n}S_{k,n} + Z_{m,n} \quad (9)$$

Subsequently, the received signals from all M RUs are collected at the DU for equalization. By adopting combining techniques and channel estimation, the estimated PUSCH modulated symbols $\hat{S}_{k,n}$ transmitted from the k-th UE through the n-th subcarrier is calculated by

$$\begin{aligned}\hat{S}_{k,n} &= \mathbf{W}_{k,n}\mathbf{Y}_n = \sqrt{p_k}\mathbf{W}_{k,n}\mathbf{G}_{k,n}S_{k,n} \\ &\quad + \sum_{i\neq k}^{K} \sqrt{p_i}\mathbf{W}_{k,n}\mathbf{G}_{i,n}S_{i,n} + \mathbf{W}_{k,n}\mathbf{Z}_n\end{aligned}$$

where $\mathbf{W}_{k,n} \in \mathbb{C}^{1\times M}$ is the weight vector decided by different combining techniques, $\mathbf{Y}_n = [Y_{1,n}, \ldots, Y_{M,n}]^{\mathrm{T}}$ represents the received signals of M RUs on the n-th subcarrier, $\mathbf{G}_{k,n} = [G_{1k,n}, \ldots, G_{Mk,n}]^{\mathrm{T}}$, and the noise vector $\mathbf{Z}_n = [Z_{1,n}, \ldots, Z_{M,n}]^{\mathrm{T}}$. The MMSE combining vector for the CF-Equalizer in Fig. 3 is given by

$$\mathbf{W}_{k,n} = \sqrt{p_k}\mathbf{G}^{\mathrm{H}}_{k,n}\left(\sum_{i=1}^{K} p_i\mathbf{G}_{i,n}\mathbf{G}^{\mathrm{H}}_{i,n} + \frac{\sigma_Z^2}{\sigma_S^2}\mathbf{I}_M\right)^{-1} \quad (10)$$

where $\mathbf{I}_M$ is the identity matrix with the size M.

Finally, the data is successfully recovered through a detailed process that involves PUSCH Decode and ULSCH Decode, both of which are implemented using the MATLAB 5G Toolbox.

IV. Numerical Results and Discussions

This section analyzes the influence of key parameters on the performance of the CF-MIMO system. The parameters under consideration include the number of RUs (2 RUs, 4 RUs, or 8 RUs), SCS values (15 kHz, 30 kHz, 60 kHz, 120 kHz), the type of channel estimation (CE) method employed, perfect or practical, and the MCS, while assuming a noise figure of 9 dB, a TDL-B delay profile with a 30 ns delay spread, and no Doppler shift (0 Hz). Unless explicitly specified otherwise, the results presented in this section are based on configurations with 8 RUs and an SCS of 15 kHz. It is important to note that scaling to larger network sizes is not feasible in this link-level simulator due to the computational demands of full PHY-layer modeling.

Link-level performance is evaluated using BLER versus TX-SNR curves. These curves are generated by varying the average TX-SNR and measuring the BLER corresponding to each average SNR value, where the SNR range is a configurable parameter within our simulation framework. The BLER is defined as the ratio of incorrectly received blocks to the total number of transmissions. To ensure statistical precision in the reported results, simulations were performed for 2×10^5 transport block (TB) transmissions for each average TX-SNR value, with the TDL channel randomly varied for each TB. This approach ensures a sufficiently large number of independent channel realizations, resulting in reliable and representative performance metrics. While this work focuses on detailed link-level modeling, addressing scalability, fronthaul capacity, RU coordination, and synchronization challenges requires complementary system-level simulation efforts to fully assess CF-MIMO performance under realistic deployment conditions.

A. TX-SNR Definition

In uplink CF-MIMO systems, signals from a UE are received at multiple RUs over links with varying lengths and different path losses, complicating the definition of a standard SNR. Therefore, the TX-SNR is used to plot BLER curves, defined as the ratio of the transmit power per UE antenna per RE to the noise power at the receivers. It is assumed that the transmit power is uniform across all transmitters, and the noise power is defined to achieve a specified TX-SNR. Specifically, in our simulations, the transmit power P_{tx} is defined to achieve a specified TX-SNR, which depends on the FFT occupancy and noise power, following the relationship:

$$\text{TX-SNR} = P_{\text{tx}} - 10\log_{10}\left(\frac{12 \times N_{\text{SG}}}{N_{\text{fft}}}\right) - 10\log_{10}(N_0), \quad (11)$$

where N_{SG} is the number of resource blocks, N_{fft} is the FFT size, and N_0 is the noise power per receive antenna. The noise power is calculated as $N_0 = kBT_e$, where k is the Boltzmann constant, B is the bandwidth, and $T_e = T_{\text{Ant}} + 290(NF - 1)$ is the equivalent noise temperature. Furthermore, the amplitude of the transmitted signal accounts for FFT size and resource grid scaling, and the transmitter distributes power equally across all antennas, effectively simulating a unit-norm beamformer. As an illustrative example, for a noise figure of 6 dB, antenna temperature of 290 K, $N_{\text{SG}} = 25$, and $N_{\text{fft}} = 512$, a TX-SNR of 130 dB corresponds to approximately 7.58 dBm (5.73 mW) transmit power, while a TX-SNR of 85 dB corresponds to approximately –37.4 dBm (0.18 μW).

B. Large-Scale Fading Model

The 3GPP path loss model and uncorrelated shadow fading in [24] are applied to calculate the large-scale fading coefficient β_{mk} in (1)

TABLE 5. **MCS and TBS configuration in this paper (Code Rate values are scaled by 1024; PRBs indicate the number of Physical Resource Blocks; TBS refers to the Transport Block Size in bits)**

MCS	Modulation Scheme	Code Rate	PRBs	TBS
0	QPSK	30	25	208
1	QPSK	64	25	456
2	QPSK	120	25	848
3	QPSK	193	25	1352
4	QPSK	308	25	2152
5	QPSK	526	25	3752
6	QPSK	679	25	4736
7	16QAM	340	25	4736
8	16QAM	434	25	6016
9	16QAM	553	25	7808
10	16QAM	658	25	9224
11	64QAM	438	25	9224
12	64QAM	517	25	11016
13	64QAM	616	25	13064
14	64QAM	772	25	16392
15	256QAM	682.5	25	18960
16	256QAM	754	25	21000
17	256QAM	841	25	23568
18	256QAM	948	25	26632

$$\beta_{mk} = 10^{\frac{\text{PL}_{mk} + \text{SF}_{mk}}{10}} \quad (12)$$

where PL_{mk} denotes the path loss, and $\text{SF}_{mk} \sim \mathcal{N}(0, \sigma_{SF}^2)$ is the shadow fading. We consider a urban microcell (UMi) scenario with the non-line-of-sight (NLOS) propagation, in which the height of the RU antenna $h_{RU} = 10$ m, the height of UE antenna $h_{UE} = 1.65$ m and the carrier frequency $f_c = 1.9$ GHz. The path loss in dB is given by [24]

$$\text{PL}_{mk} = \max(\text{PL}_{mk,LOS}, \text{PL}_{mk,NLOS}) \quad (13)$$

where

$$\begin{aligned}\text{PL}_{mk,NLOS} &= 35.3\text{log}_{10}(d_{mk,3D}) + 22.4 \\ &\quad + 21.3\text{log}_{10}(f_c) - 0.3(h_{UE} - 1.5)\end{aligned} \quad (14)$$

and

$$\text{PL}_{mk,LOS} = \begin{cases} \text{PL}_1 & 10\text{m} \le d_{mk,2D} \le d_{BP}^{'} \\ \text{PL}_2 & d_{BP}^{'} \le d_{mk,2D} \le 5\text{km} \end{cases} \quad (15)$$

where $\text{PL}_1 = 32.4 + 21\text{log}_{10}(d_{mk,3D}) + 20\text{log}_{10}(f_c)$ and $\text{PL}_2 = 32.4 + 40\text{log}_{10}(d_{mk,3D}) + 20\text{log}_{10}(f_c) - 9.5\text{log}_{10}((d_{BP}^{'})^2 + (h_{RU} - h_{UE})^2)$. $d_{mk,2D}$ is the distance between the bottom of the k^{th} UE and the m^{th} RU while $d_{mk,3D}$ denotes the distance between the top of both antennas. $d_{BP}^{'} = 4(h_{RU} - h_E)(h_{UE} - h_E)f_c/c$ represents the breakpoint distance, where $h_E = 1$ m is the effective environment height. Note that f_c is in Hz only for this equation, and c is the propagation velocity in free space. The standard deviation of shadow fading $\sigma_{SF} = 7.82$ dB [3].

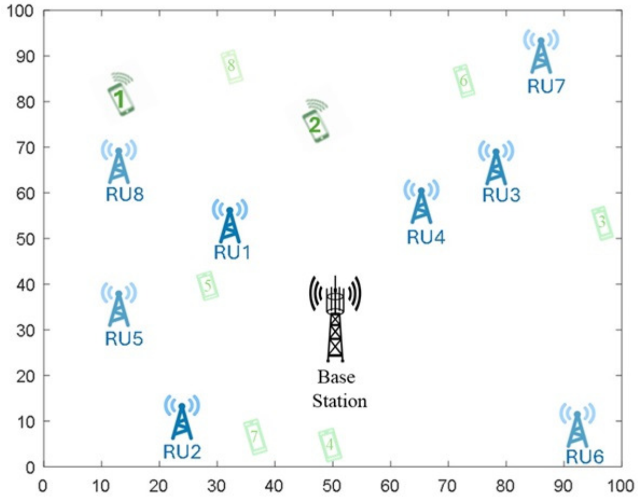

FIGURE 5. **A system setup with fixed locations for a BS, UEs, and RUs within a $100\mathrm{m} \times 100\mathrm{m}$ simulation area. In all results, only UE1 and UE2 are considered, except in Subsection K where additional UEs (UE3 to UE8) are included. UEs are serviced either by the distributed RUs (2 RUs, or 4 RUs or 8RUs) or the collocated antennas (2 or 4 or 8 antennas) at BS.**

C. Parameters and Setup

For generating the BLER plots, the UE positions were initially randomized but then fixed across all simulations, as depicted in Fig. 5. The simulation setup considers a square area of $100\mathrm{m} \times 100\mathrm{m}$, where two single-antenna UEs are served by multiple RUs, each equipped with one antenna (unless otherwise specified). Specifically, for configurations with 2 RUs, only RU1 and RU2 are utilized, while the first four RUs are selected for the 4 RU case. When comparing with co-located MIMO, we assume that the base station (BS), as shown in this figure, is equipped with 2, 4, or 8 antennas.While larger antenna and UE configurations are certainly of great interest—particularly in the context of massive MIMO—the main objective of this work is to establish a fully 3GPP-compliant link-level simulation framework for CF systems and to evaluate BLER performance under realistic conditions. This process is computationally intensive, and even the current setup required the use of high-performance computing (HPC) resources to complete the simulations. Expanding to larger-scale scenarios by developing accurate PHY-abstraction models—without the need to implement the full physical layer processing chain—is part of our ongoing and future research.

Furthermore, the MCSs employed in the simulations, which are selected from [24], are listed in Table 5. It's worth mentioning that each MCS level corresponds to a different combination of modulation order and LDPC coding rate. In our previous work [28], we've evaluated required SINR for given BLER on the AWGN channel by extensive link simulations using the range of 5G NR MCSs. This consistent setup ensures comparability across all scenarios and results.

D. Analysis and Demonstration of Results for Different MCS

Fig. 6 presents the BLER versus TX-SNR curves for a CF-MIMO system with 8 RUs and 2 UEs, illustrating the performance across a range of MCS. The two subplots represent the performance for **UE 1** and **UE 2**, respectively, covering MCS indices from 0 to 18, mapped to specific modulation schemes: QPSK (indices 0–6), 16-QAM (indices 7–10), 64-QAM (indices 11–14), and 256-QAM (indices 15–18). Each set of curves demonstrates the BLER's dependence on TX-SNR, highlighting the trade-off between SNR requirements and modulation efficiency.

In the *top subplot*, representing UE 1, the QPSK-based MCS (0–6) achieves robust performance at low TX-SNR values (72–87 dB) with acceptable BLER, albeit at lower spectral efficiency. As the MCS increases, transitioning to 16-QAM (indices 7–10) and 64-QAM (indices 11–14), the required TX-SNR for achieving BLER $< 10^{-2}$ progressively shifts toward higher values, reflecting the higher SNR demand for these more spectrally efficient modulations. Finally, for 256-QAM (indices 15–18), the TX-SNR requirement further increases (105–115 dB), emphasizing the trade-off for achieving maximum spectral efficiency under favorable channel conditions. Similarly, in the *bottom subplot* for UE 2, the trends follow a comparable pattern, with slight variations due to channel differences between the two UEs. The smooth decline of BLER curves across all modulation schemes demonstrates the CF-MIMO system's reliability and adaptability to varying channel conditions and user requirements. While system-level simulations with many users per base station can provide statistical performance measures, such as CDFs, offering a broader view of overall network behavior, our link-level simulations focus on detailed, user-specific performance under controlled radio conditions. As shown in Figure 5, UE 1 is located closer to the RUs, particularly RU 8, which provides slightly better performance results compared to UE 2. This is evident at comparable TX-SNR points; for instance, at TX-SNR = 69 dB and MCS 0, UE 1 achieves a BLER of 0.14, whereas UE 2 reaches a BLER of 0.42. Similarly, at TX-SNR = 108 dB and MCS 18, UE 1 achieves a BLER of 0.07, while UE 2 requires the same TX-SNR to reach a BLER of 0.14. This proximity leads to improved channel quality, enabling lower BLER values at equivalent TX-SNR levels, as reflected in the curves for UE 1. The figure effectively showcases the scalability of the CF-MIMO system's performance across a wide range of SNR values and modulation schemes, reinforcing its suitability for diverse uplink scenarios with heterogeneous user requirements. As a direction for future work, one may consider the case where the MCS level is adaptively selected based on the position and channel conditions specific to each UE.

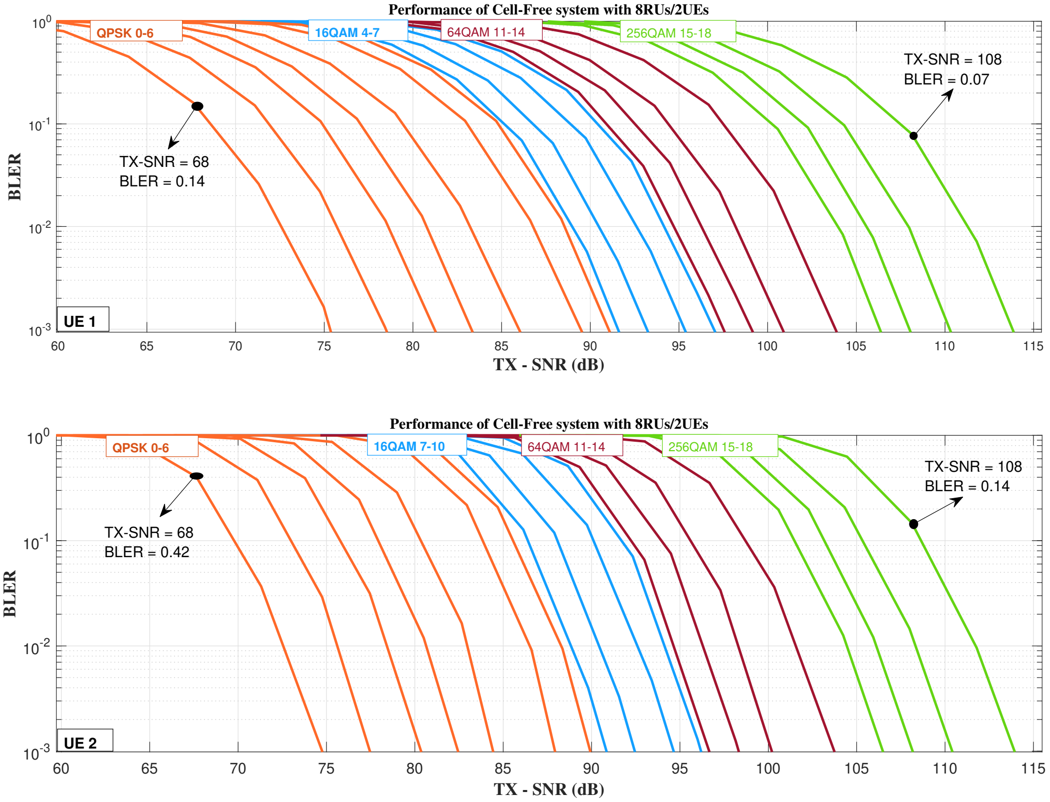

FIGURE 6. **BLER-SNR curves for MCS 0-18 (left to right) for CF-MIMO system with 8 RUs and 2 UEs. The top plot shows results for UE 1, while the bottom plot shows results for UE 2.**

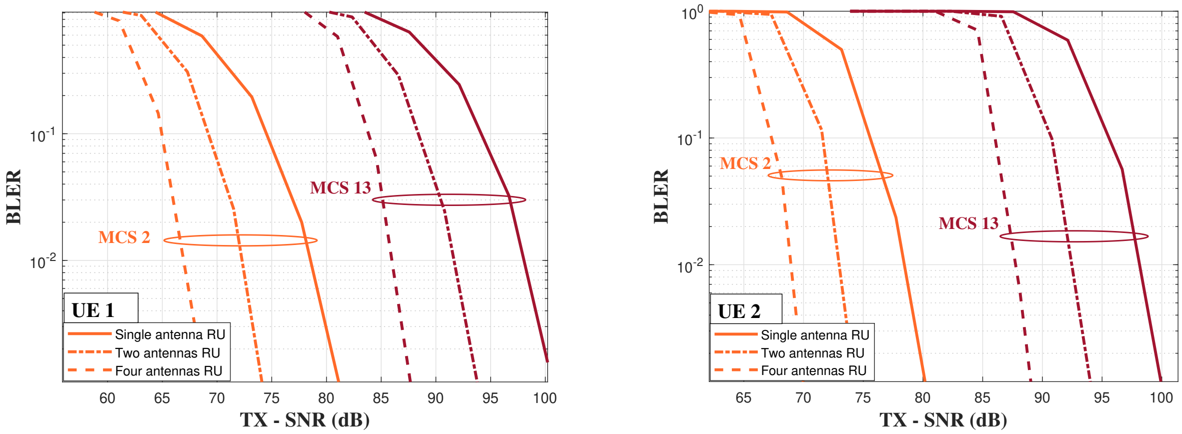

FIGURE 7. **BLER versus TX-SNR curves for CF-MIMO system with 8 RUs and 2 UEs, with different MCS (MCS 2 and 13), comparing performance across varying numbers of RU antennas. The left plot shows results for UE 1, while the right plot shows results for UE 2.**

E. Evaluating the Effect of Varying the Number of RU's antenna on BLER

Fig. 7 illustrates the BLER-SNR performance of the CF-MIMO system for UE 1 and UE 2, focusing on the impact of varying the number of antennas per RU. The evaluation is conducted for two selected MCS indices—MCS 2 (QPSK) and MCS 13 (64-QAM)—to capture performance across different modulation and coding schemes. The solid lines represent RUs with a single antenna, while the dot-dash and dashed lines correspond to RUs equipped with 2 and 4 antennas, respectively. As observed, increasing the number of antennas per RU significantly improves BLER performance for both UEs. For MCS 2, the performance gains are more pronounced at lower SNR values, reflecting better link robustness in challenging conditions. For MCS 13, which requires higher SNR to achieve reliable decoding, the benefits of additional antennas are evident in the noticeable leftward shift of the BLER curves, particularly for UE 1. This indicates that enhanced spatial diversity and signal power aggregation from multiple antennas per RU contribute to improved decoding capability. Overall, the results confirm

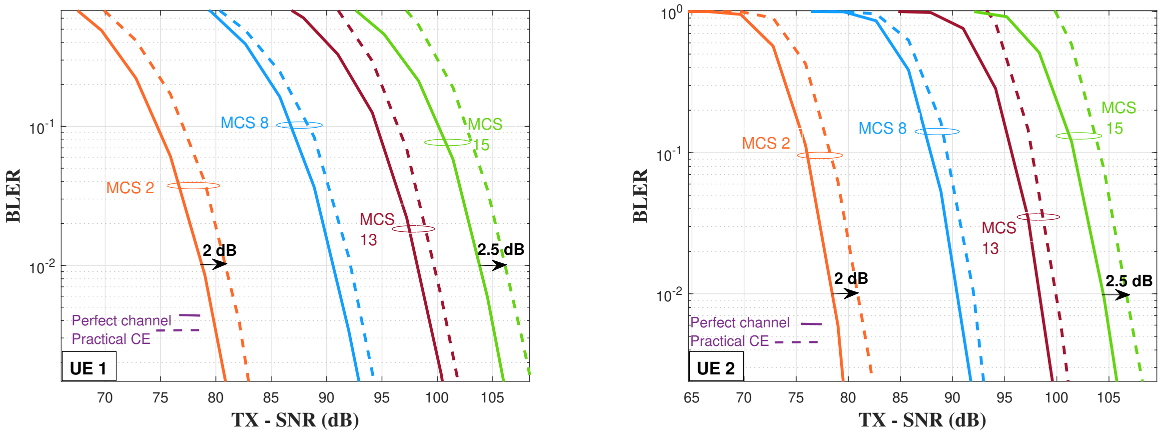

FIGURE 8. BLER versus TX-SNR curves for UE1 (a) and UE2 (b) with different MCS (MCS 2, 8, 13, and 15), comparing performance under perfect channel conditions and practical channel estimation (CE).

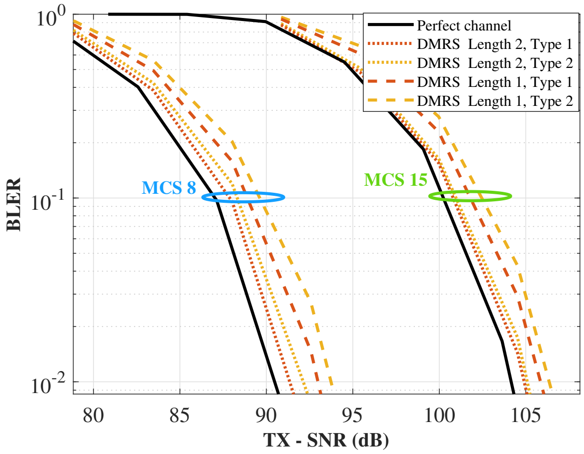

FIGURE 9. BLER versus TX-SNR curves for UE 1 under different DMRS configurations (Type 1 and Type 2, lengths 1 and 2) for MCS 8 and MCS 15, compared against the perfect channel baseline.

that equipping RUs with multiple antennas can effectively enhance system performance across a range of MCS levels.

F. Evaluating the Impact of Practical Channel Estimation on BLER curves

Figures 8 and 9 illustrate the BLER versus TX-SNR performance of the CF-MIMO system, focusing on the impact of practical CE under different configurations and scenarios. Fig. 8 illustrates results for UE1 and UE2 using selected MCS indices (2, 8, 13, and 15), covering modulation schemes from QPSK to 256-QAM. The solid curves represent the system performance under perfect channel knowledge, while the dashed curves show the performance under practical channel estimation, where estimation imperfections arise due to noise and limited pilot resources. These results were obtained using the standard DMRS Type 2 configuration with length 2. For both UEs, it is evident that practical channel estimation results in a slight degradation in performance compared to the ideal case, as indicated by the horizontal shift of the BLER curves towards higher TX-SNR values, with an approximate difference of 2 dB. This degradation is more pronounced for 256-QAM, where the difference is approximately 2.5 dB, as higher modulation orders are inherently more sensitive to channel imperfections. Despite this, the CF-MIMO system maintains a reliable performance under practical channel estimation, with BLER values converging to acceptable levels as the TX-SNR increases. This indicates the system's robustness and suitability for deployment in real-world environments where perfect channel knowledge is not available. The comparison between UE 1 and UE 2 further highlights the channel-dependent variations in performance, reinforcing the importance of effective channel estimation in CF-MIMO systems. In [23], the use of DMRS is comprehensively explained, highlighting the four different types of DMRS configurations based on their density and length. In this work, we specifically focus on one particular DMRS configuration for our analysis. However, we believe that there is significant potential for further exploration in this area. Future studies could investigate the performance of different DMRS configurations in various scenarios, particularly in the context of CF-MIMO systems. This includes analyzing the impact of DMRS density and length under varying channel conditions, such as high Doppler shifts and different delay spread profiles, which are common in practical environments. Extending this work to include such considerations would provide deeper insights into the optimization of DMRS configurations and their effect on system performance in CF deployments, and we plan to explore these aspects in our future research.

Building on this, Fig. 9 extends the evaluation by comparing the system's BLER performance under various DMRS configurations. Specifically, we analyze Type 1 and Type 2 DMRS patterns with both length 1 and length 2, focusing on MCS 8 and MCS 15. The figure highlights how the choice of DMRS type and density impacts channel estimation quality, showing performance differences relative to the perfect channel baseline. Specifically, Type 1 DMRS occupies every other resource element, providing a denser

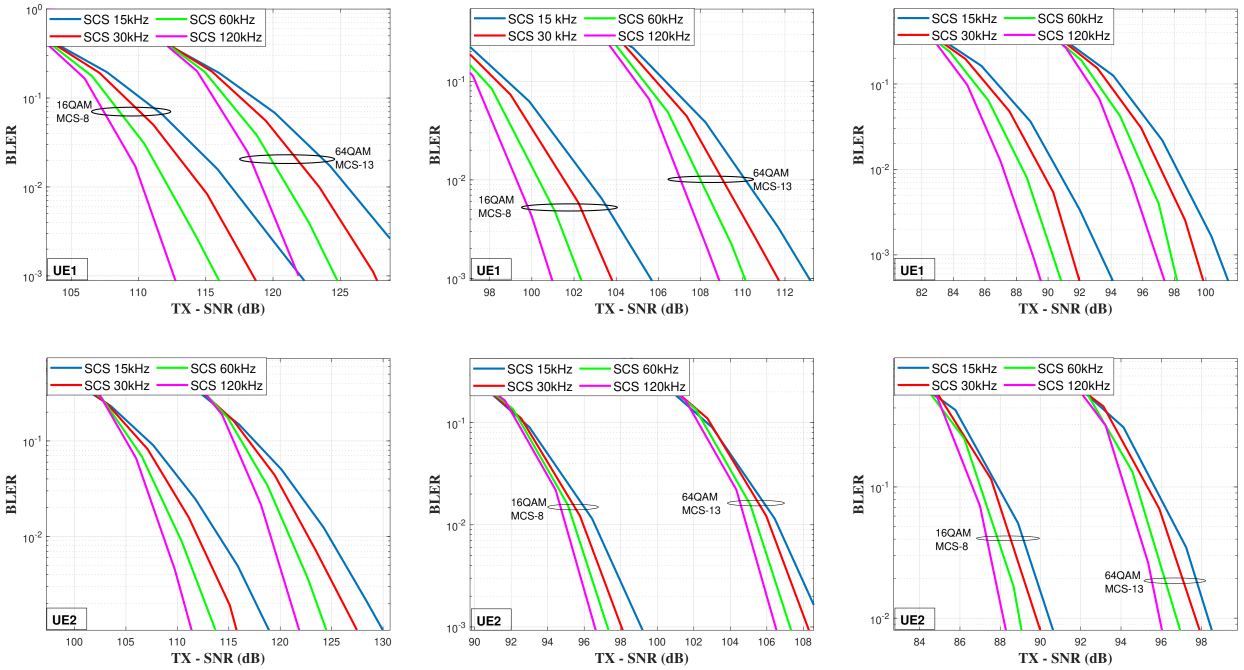

(a) Configuration 1 with 2RUs (b) Configuration 2 with 4RUs (c) Configuration 3 with 8RUs

FIGURE 10. BLER versus TX-SNR curves for UE1 (top plot) and UE2 (lower plot) with MCS 8 (16-QAM) and MCS 13 (64-QAM) across three configurations (2 RUs, 4 RUs, and 8 RUs) and four subcarrier spacings (15 kHz, 30 kHz, 60 kHz, and 120 kHz), showcasing the combined effects of RU deployment and SCS on system performance and frequency diversity.

pilot pattern, while Type 2 DMRS occupies every third pair of resource elements, resulting in lower pilot density. As expected, Type 1 generally offers better BLER performance due to its higher pilot density, which improves estimation accuracy — an effect clearly observed in the figure. Notably, while increasing the DMRS length further improves estimation robustness, the choice between Type 1 and Type 2 patterns still significantly affects the balance between pilot overhead and achievable accuracy, especially at higher-order MCS. Together, Figures 8 and 9 demonstrate that both practical channel estimation effects and DMRS configuration choices play significant roles in determining the overall BLER performance of CF-MIMO systems, emphasising the need for careful pilot design in real-world deployments.

G. Evaluating the Effect of Signal Bandwidth by Varying Subcarrier Spacing from 15 to 120 kHz

Fig. 10 illustrates the impact of SCS on the performance of the CF-MIMO system, focusing on the bandwidth of the transmitted signals. The results are shown for the perfect channel estimation scenario, providing a baseline for evaluating the effect of different SCS values on system performance. The BLER-SNR performance is evaluated for two modulation and coding schemes (MCS 8 and 13) and for three system configurations (2 RUs, 4 RUs, and 8 RUs) with four different SCS values: 15 kHz, 30 kHz, 60 kHz, and 120 kHz. By increasing the SCS from 15 kHz to 120 kHz, the bandwidth of the signals increases proportionally, ranging from 4.5 MHz to 36 MHz. Given the channel's delay spread of 30 ns, the approximate coherence bandwidth is 5.5 MHz, which plays a critical role in understanding the system's frequency diversity.

As evident in the figure, increasing the SCS improves performance due to enhanced frequency diversity. When the total bandwidth occupied by a codeword exceeds the coherence bandwidth (e.g., for higher SCS values such as 30 kHz, 60 kHz, or 120 kHz), multiple subcarriers may experience uncorrelated fading, allowing the system to exploit frequency diversity. This results in improved reliability and lower BLER at a given TX-SNR. For both UE 1 and UE 2, the trends confirm these conclusions, with higher SCS values consistently leading to steeper BLER curves and reduced TX-SNR requirements for achieving low BLER levels. Moreover, the effect of increasing SCS is observed across all configurations. In Configuration 3 (with 8 RUs), the performance improvement is particularly pronounced due to better spatial diversity in combination with frequency diversity. The consistency of this trend across both UEs underscores the robustness of the CF-MIMO system in exploiting frequency diversity through higher SCS values. This analysis highlights the importance of matching the SCS to the channel conditions, particularly the coherence bandwidth, to maximize system performance.

It is also worth noting that although the overall performance improves with 8 RUs, the performance gain from increasing the SCS is less significant compared to the case

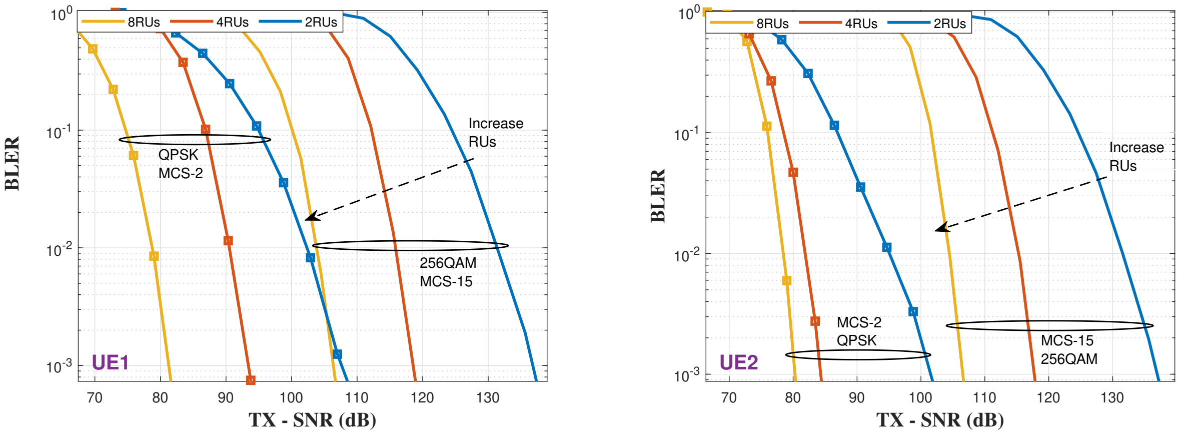

FIGURE 11. **BLER versus TX-SNR performance for UE1 and UE2 with varying numbers of RUs (2, 4, and 8) for MCS 2 (QPSK) and MCS 15 (256-QAM), highlighting the impact of increased RUs on spatial diversity and proximity to RUs. The left plot shows results for UE 1, while the right plot shows results for UE 2.**

with fewer RUs—for example, the TX-SNR improvement for UE1 is around 5 dB with 8 RUs, versus approximately 10 dB with 2 RUs. This is expected, as the system already benefits from spatial diversity with a higher number of RUs, making additional gains from frequency diversity less pronounced.

H. Evaluating the Effect of Varying the Number of RUs on BLER

Figure 11 highlights the impact of increasing the number of RUs on the BLER-SNR performance for UE 1 and UE 2. Increasing the number of RUs offers two key benefits: (1) enhanced spatial diversity, which improves reliability by utilizing multiple propagation paths, and (2) an increased likelihood of a UE being physically closer to one or more RUs, a phenomenon often referred to as "site diversity" [29], resulting in better channel conditions and improved overall performance. By examining the RU locations in the accompanying layout (5), it is evident how the spatial configuration affects the performance of each UE differently.

For UE 2, increasing the number of RUs from 2 to 4 results in significant improvement due to its proximity to RUs in the 4-RU configuration, particularly RU 4. This closer proximity reduces path loss and enhances signal quality, which is clearly reflected in the performance improvement from 2 RUs to 4 RUs. However, for UE 1, the most noticeable improvement occurs when the number of RUs increases from 4 to 8. In the 8-RU configuration, UE 1 becomes significantly closer to RU 8, leveraging site diversity, where the specific spatial arrangement of RUs relative to UEs offers additional diversity gains. This trend illustrates that the benefits of adding RUs are configuration-dependent, with different UEs experiencing varying degrees of diversity improvement based on their relative location to the RUs.

For both UEs, increasing the number of RUs from 2 to 4 results in steeper BLER curves, indicating enhanced spatial diversity. In contrast, increasing the number of RUs from 4 to 8 shifts the curves to the left without affecting their slope, as the improvement is primarily attributed to enhanced site diversity. This analysis underscores the importance of spatial diversity and proximity in CF-MIMO systems, with each configuration offering unique advantages for different UEs. Exploring this concept further, particularly the interplay between site diversity and system configuration, will be a key focus of our future work to optimize performance under diverse deployment scenarios.

I. Impact of Co-Located vs Distributed Antenna Configurations on BLER

Figure 12 examines the BLER-SNR performance for UE 1 and UE 2, focusing on the differences between co-located[1] and distributed antenna configurations under MCS 8 (16QAM) with varying numbers of antennas (2, 4, and 8). While the co-located configuration centralizes all antennas at the BS, the distributed configuration, as shown in Fig. 5, employs spatially distributed RUs, each equipped with one antenna. For 2 antennas, it can be observed that the co-located configuration performs better for both UE 1 and UE 2, with a more significant performance gap observed for UE 2. This difference can be attributed to the specific locations of the UEs, RUs (RU1 and RU2), and the BS. In this case, the co-located configuration benefits from centralized processing at the BS, which provides stronger and more consistent signals to both UEs compared to the distributed setup with only two RUs.

As the number of antennas increases from 2 to 8, the distributed configuration shows significant improvement in performance for both UEs, with the BLER curves shifting to lower SNR values. However, for the co-located setup with 8 antennas, the curve becomes steeper than that of the distributed configuration. This is because the spatial diversity in the co-located case is higher with all antennas centrally

---

[1] We note that the co-located antenna system serves as the baseline for traditional MIMO performance.

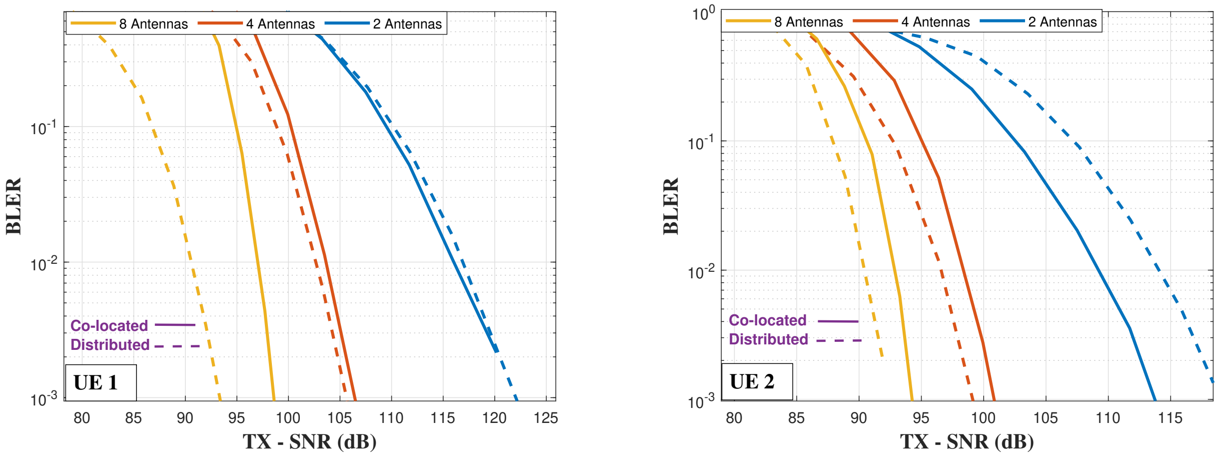

FIGURE 12. BLER versus TX-SNR performance for UE1 and UE2 with varying numbers of antennas (2, 4, and 8) for MCS 8 (16QAM), comparing the performance of the co-located and distributed configurations. The left plot shows results for UE 1, while the right plot shows results for UE 2.

aggregated, resulting in more effective multi-antenna processing for the UEs located nearby. As a representative quantitative example at BLER = 10^{-2}, we observe that with 2 antennas, the co-located configuration outperforms the distributed one by approximately 0.8 dB for UE1 and 4.1 dB for UE2. In contrast, with 8 antennas, the distributed setup shows better performance, outperforming the co-located case by 7.1 dB and 3.5 dB for UE1 and UE2, respectively. These values, summarized in Table 6, help illustrate how performance trends depend on both antenna count and deployment layout.

It is important to emphasize that the presented results are specific to the selected topology, including fixed UE, RU, and BS locations. While this controlled setup allows for detailed analysis and clear interpretation of performance trends, it also introduces limitations in terms of generalizability. Specifically, the observed SNR advantages depend strongly on the spatial relationships between UEs and RUs. In practical systems, user and RU locations vary significantly, and the performance gains from distributed configurations may differ under randomized or dynamic topologies. Therefore, while the current results provide valuable insight into the influence of antenna distribution, they should be interpreted as specific to this layout. To ensure a fair comparison, spatial correlation effects were excluded from this study. As a next step, we aim to extend the simulator to support randomized topologies and aggregate performance metrics, enabling a more generalized and statistically robust analysis.

TABLE 6. Difference in Required TX-SNR Between Distributed and Co-located Configurations at BLER = 10^{-2}.

Total no. of antennas	Δ SNR (UE1, dB)	Δ SNR (UE2, dB)
2	+0.8	+4.1
4	–1.1	–1.8
8	–7.1	–3.5

J. Evaluation of Carrier Frequency Impact

Figure 13 presents the BLER versus TX-SNR performance for UE1 and UE2 under MCS 2 (QPSK), comparing the results at two carrier frequencies: 3.6 GHz and 1.9 GHz. The figure clearly illustrates how increasing the carrier frequency affects system performance. Specifically, we observe that the BLER curves at 3.6 GHz shift rightward compared to those at 1.9 GHz for both UEs, indicating that a higher TX-SNR is required to achieve the same BLER target at the higher frequency. This degradation is mainly due to increased path loss at 3.6 GHz, which negatively impact the received signal quality.

K. Impact of Varying Number of UEs on BLER Performance

To further strengthen the evaluation, we extended our simulations to study the effect of varying the number of UEs on system performance under the same setup with 8 RUs. Fig. 14 presents the BLER versus TX-SNR curves for different numbers of UEs, ranging from a single UE up to eight UEs, using the same RU configuration and system parameters. The results show that, as the number of UEs increases, the BLER performance slightly degrades due to increased multi-user interference. With a single UE, there is no interference, and the available spatial and frequency resources are fully dedicated to that user. However, as the number of UEs grows, multiple users share the same time-frequency resources, increasing interference within the system. This leads to slightly higher SNR requirements to maintain the same BLER target across all users. Nevertheless, the CF-MIMO system maintains reliable performance even as the UE count increases to eight, demonstrating its scalability and robustness in supporting multi-user environments. These findings highlight the importance of evaluating multi-UE performance to better understand the capacity and limits of CF-MIMO systems, complementing the single-UE and two-UE evaluations presented in earlier sections.

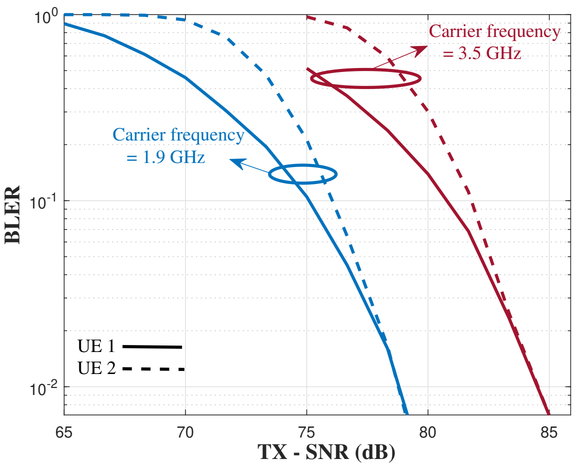

FIGURE 13. **Impact of carrier frequency on BLER versus TX-SNR performance for UE1 and UE2 under MCS 2 (QPSK), comparing results between 3.6 GHz and 1.9 GHz.**

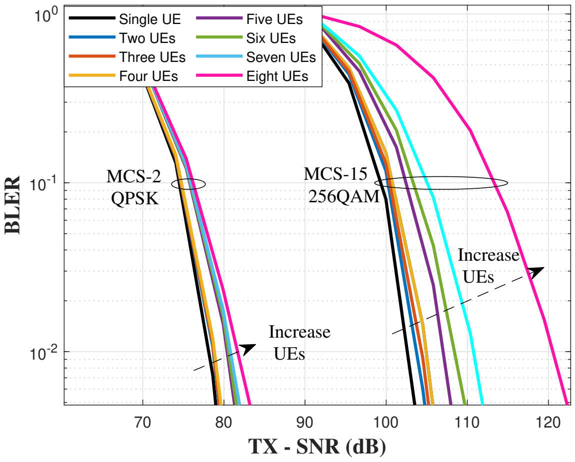

FIGURE 14. **BLER versus TX-SNR performance under varying numbers of UEs (from 1 to 8) with 8 RUs, showing the impact of increasing UE density and multi-user interference on system performance. Results are shown for UE1 under MCS 2 (QPSK) and MCS 15 (256 QAM).**

L. Spectral Efficiency Analysis Based on BLER Results

To provide a clearer view of the practical performance impact beyond BLER, we present a spectral efficiency analysis derived from the link-level results. This addition bridges the gap between physical-layer reliability and system-level throughput by mapping each MCS level to its corresponding spectral efficiency (in bits/s/Hz), and associating it with the TX-SNR required to achieve a target BLER of 10^{-2}. Figure 15 shows the resulting Spectral Efficiency vs. TX-SNR curves for both the distributed CF-MIMO and the co-located MIMO configurations. As expected, the CF-MIMO system achieves higher spectral efficiency at a given TX-SNR due to its spatial and site diversity advantages, offering approximately 1–2 bits/s/Hz more than the co-located configuration at TX-SNRs above 90 dB.

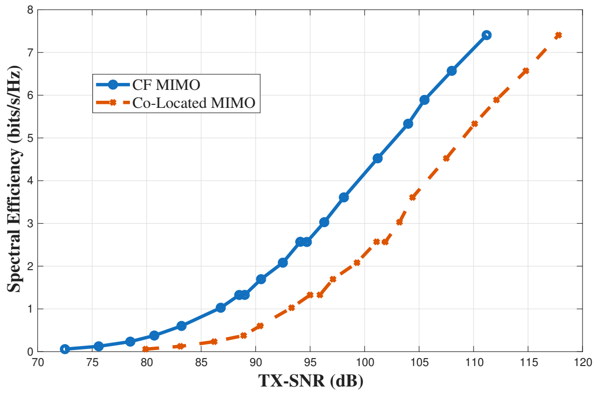

FIGURE 15. **Spectral efficiency (bits/s/Hz) versus TX-SNR (dB) for CF-MIMO and co-located MIMO setups. Each MCS level is mapped to its spectral efficiency, and the TX-SNR corresponds to the point at which a BLER of 10^{-2} is achieved.**

V. Discussion, Scalability, and Future Work

A. Scalability and Fronthaul Considerations

Beyond the link-level results presented in this work, scaling CF-MIMO to practical deployments introduces important system-level considerations. While a full evaluation of these aspects is left for future work, we outline several key factors—such as fronthaul capacity, synchronization overhead, and RU processing complexity—that are critical to realizing the performance gains of CF-MIMO at scale.

Fronthaul Overhead:

In CF-MIMO, each RU must transmit received baseband I/Q samples to the CPU. For uplink transmission, the required fronthaul data rate R_f scales approximately as:

$$R_f = N_{\text{ant}} \times B \times R_s \times q \times 2, \qquad (16)$$

where N_{ant} is the number of RU antennas, B is the bandwidth, R_s is the sampling rate per Hz (typically ≥ 2), and q is the number of quantization bits per I or Q component (e.g., 10–12 bits). Since each complex baseband sample consists of two components the total fronthaul bit rate includes a factor of 2 to account for both. For example, with $B = 100\,\text{MHz}$, $N_{\text{ant}} = 1$, $R_s = 2$, and $q = 12$ bits, the uplink fronthaul data rate is approximately:

$$R_f = 1 \times 100 \times 10^6 \times 2 \times 12 \times 2 = 4.8\text{Gbps} \qquad (17)$$

In practice, additional protocol overhead (e.g., line coding, framing, control information) can increase the required fronthaul rate [30]. To address this challenge, our recent work in [31] extends the link-level simulator used in this paper to evaluate uplink fronthaul compression methods in O-RAN–based distributed MIMO systems. We apply standardized O-RAN compression techniques to reduce the fronthaul load with minimal impact on system performance, as demonstrated by BLER curves. These findings underscore the potential of practical compression schemes to make CF-MIMO more scalable under realistic deployment constraints.

Synchronization and Coordination:

Distributed RUs require tight time [32] and frequency [33] synchronization to coherently combine signals. This introduces overhead for distributing timing information and potentially GPS- or PTP-based synchronisation, depending on deployment density and backhaul constraints.

RU-Side Processing Complexity:

In this study, RU functionality is limited to RF, ADC, and FFT/iFFT. However, more scalable CF architectures may push part of the PHY processing (e.g. channel estimation) to the RUs to reduce fronthaul load. This offloading reduces central load but increases RU hardware requirements and coordination complexity. While detailed quantification is left for future system-level analysis, these considerations are critical in assessing the viability of large-scale CF-MIMO systems. Trade-offs between fronthaul capacity, RU capability, and coordination complexity must be carefully balanced during deployment design.

B. Future Work

Future work will extend the current link-level simulator to support downlink transmission in CF-MIMO systems, including multi-antenna RUs transmitting multi-layer streams. We will also investigate channel estimation under more challenging conditions, such as high Doppler shifts, large delay spreads, and pilot contamination from reuse, with a focus on robust DMRS design. The simulator will be enhanced to study synchronization issues and the impact of time and frequency offsets across spatially distributed RUs—key factors that affect coherent transmission in practical deployments. Addressing these non-idealities will provide clearer insight into system design and performance limits. Additional directions include evaluating the effects of RU correlation and shadow fading, as well as developing algorithms for RU placement to improve site diversity. We also plan to adopt more realistic deployment models, such as hexagonal layouts or random RU/UE positioning, to improve generalizability. Lastly, future evaluations will consider user mobility, heterogeneous distributions, and inter-cell interference to assess scalability under practical conditions.

VI. Conclusion

In this work, we developed and applied a comprehensive, 3GPP-compliant link-level simulator to evaluate the PHY-layer performance of uplink CF-MIMO systems under 5G NR standards. Through systematic simulations, we analyzed key parameters such as SCS, MCS, the number of distributed RUs, and the number of RU antennas, using BLER as the primary performance metric. The results demonstrated that increasing the number of RUs enhances spatial diversity and reduces path loss, leading to improved BLER performance. We showed that higher SCS values effectively leverage frequency diversity, particularly when the signal bandwidth exceeds the coherence bandwidth of the channel. Furthermore, we evaluated multiple DMRS configurations and confirmed that Type 1 with length 2 provides superior channel estimation performance under practical conditions. Importantly, we compared the CF-MIMO system with a co-located antenna system (representing a traditional MIMO baseline) and confirmed that the CF-MIMO configuration consistently achieves better performance due to its spatial distribution advantages. Overall, this study provides valuable insights into the spatial, frequency, and estimation aspects of CF-MIMO system design, offering guidance for MCS adaptation and enabling accurate PHY abstraction for higher-layer simulations.

REFERENCES

[1] H. Ahmadi, M. Rahmani, S. B. Chetty, E. E. Tsiropoulou, H. Arslan, M. Debbah, and T. Quek, "Towards sustainability in 6G and beyond: Challenges and opportunities of open RAN," *arXiv preprint arXiv:2503.08353*, 2025.

[2] H. Q. Ngo, A. Ashikhmin, H. Yang, E. G. Larsson, and T. L. Marzetta, "Cell-free massive MIMO versus small cells," *IEEE Transactions on Wireless Communications*, vol. 16, no. 3, pp. 1834–1850, 2017.

[3] E. Björnson and L. Sanguinetti, "Scalable cell-free massive MIMO systems," *IEEE Transactions on Communications*, vol. 68, no. 7, pp. 4247–4261, 2020.

[4] X. Lin, J. Li, R. Baldemair, J.-F. T. Cheng, S. Parkvall, D. C. Larsson, H. Koorapaty, M. Frenne, S. Falahati, A. Grovlen *et al.*, "5G new radio: Unveiling the essentials of the next generation wireless access technology," *IEEE Communications Standards Magazine*, vol. 3, no. 3, pp. 30–37, 2019.

[5] Ö. T. Demir, E. Björnson, L. Sanguinetti *et al.*, "Foundations of user-centric cell-free massive MIMO," *Foundations and Trends® in Signal Processing*, vol. 14, no. 3-4, pp. 162–472, 2021.

[6] F. Göttsch, N. Osawa, T. Ohseki, K. Yamazaki, and G. Caire, "Subspace-based pilot decontamination in user-centric scalable cell-free wireless networks," *IEEE Transactions on Wireless Communications*, vol. 22, no. 6, pp. 4117–4131, 2022.

[7] M. Rahmani, M. Bashar, M. J. Dehghani, A. Akbari, P. Xiao, R. Tafazolli, and M. Debbah, "Deep reinforcement learning-based sum rate fairness trade-off for cell-free mMIMO," *IEEE Transactions on Vehicular Technology*, vol. 72, no. 5, pp. 6039–6055, 2022.

[8] S. Mohammadzadeh, M. Rahmani, K. Cumanan, A. Burr, and P. Xiao, "Pilot and data power control for uplink cell-free massive mimo," *arXiv preprint arXiv:2502.19282*, 2025.

[9] J. Zheng, J. Zhang, E. Björnson, and B. Ai, "Impact of channel aging on cell-free massive MIMO over spatially correlated channels," *IEEE Transactions on Wireless Communications*, vol. 20, no. 10, pp. 6451–6466, 2021.

[10] W. Jiang and H. D. Schotten, "Impact of channel aging on zero-forcing precoding in cell-free massive MIMO systems," *IEEE Communications Letters*, vol. 25, no. 9, pp. 3114–3118, 2021.

[11] G. Femenias and F. Riera-Palou, "Cell-free massive MIMO-OFDM over spatially correlated doubly selective channels," *IEEE Access*, vol. 10, pp. 118 438–118 453, 2022.

[12] W. Jiang and H. D. Schotten, "Opportunistic AP selection in cell-free massive MIMO-OFDM systems," in *IEEE 95th Vehicular Technology Conference*. IEEE, 2022, pp. 1–5.

[13] J. Zheng, J. Zhang, E. Björnson, Z. Li, and B. Ai, "Cell-free massive MIMO-OFDM for high-speed train communications," *IEEE Journal on Selected Areas in Communications*, vol. 40, no. 10, pp. 2823–2839, 2022.

[14] W. Jiang and H. D. Schotten, "Cell-free massive MIMO-OFDM transmission over frequency-selective fading channels," *IEEE Communications Letters*, vol. 25, no. 8, pp. 2718–2722, 2021.

[15] H. Ge, N. Garg, and T. Ratnarajah, "Channel estimation for generalized superimposed cell-free massive MIMO-OFDM systems," in *2022 IEEE 23rd International Workshop on Signal Processing Advances in Wireless Communication (SPAWC)*. IEEE, 2022, pp. 1–5.

[16] Y. Al-Eryani, M. Akrout, and E. Hossain, "Multiple access in cell-free networks: Outage performance, dynamic clustering, and deep reinforcement learning-based design," *IEEE Journal on Selected Areas in Communications*, vol. 39, no. 4, pp. 1028–1042, 2020.

[17] S. Kurma, K. Singh, P. K. Sharma, C.-P. Li, and T. A. Tsiftsis, "On the performance analysis of full-duplex cell-free massive mimo with user

mobility and imperfect CSI," *IEEE Transactions on Communications*, 2024.

[18] Y. Chu, M. Rahmani, J. Shackleton, D. Grace, K. Cumanan, H. Ahmadi, and A. Burr, "Testbed development: An intelligent o-RAN based cell-free MIMO network," *arXiv preprint arXiv:2502.08529*, 2025.

[19] M. Rahmani Ghourtani, J. Zhao, M. Bashar, K. Cumanan, A. G. Burr, and R. Tafazolli, "Securing 5G NR networks: Innovative artificial noise methods for protecting cell-free massive MIMO," in *2025 IEEE Wireless Communications and Networking Conference (WCNC)*. IEEE, 2025.

[20] Y. Kabalcı and M. Ali, "Throughput analysis over 5G NR physical uplink shared channels," in *2020 2nd Global Power, Energy and Communication Conference (GPECOM)*. IEEE, 2020, pp. 345–349.

[21] G. Cisek and T. P. Zieliński, "Prototyping software transceiver for the 5G new radio physical uplink shared channel," in *2019 Signal Processing Symposium (SPSympo)*. IEEE, 2019, pp. 150–155.

[22] V. Ranjbar, A. Girycki, M. A. Rahman, S. Pollin, M. Moonen, and E. Vinogradov, "Cell-free mMIMO support in the O-RAN architecture: A PHY layer perspective for 5G and beyond networks," *IEEE Communications Standards Magazine*, vol. 6, no. 1, pp. 28–34, 2022.

[23] "5G NR, Physical channels and modulation," 3rd Generation Partnership Project (3GPP), Technical Report TR 38.211, 2020, release 16.

[24] "Study on channel model for frequencies from 0.5 to 100 GHz," 3rd Generation Partnership Project (3GPP), Technical Report TR 38.901, 2022, release 17.

[25] "LTE; Evolved Universal Terrestrial Radio Access (E-UTRA); Physical channels and modulation," 3rd Generation Partnership Project (3GPP), Technical Specification TS 36.211, 2016, release 14.

[26] "Technical Specification Group Radio Access Network; NR; Physical channels and modulation," 3rd Generation Partnership Project (3GPP), Technical Specification TS 38.211, 2017, release 15.

[27] "User Equipment (UE) Radio Transmission and Reception," 3rd Generation Partnership Project (3GPP), Technical Specification TS 36.101, 2016, release 15.

[28] L. Méndez-Monsanto, A. MacQuarrie, M. R. Ghourtani, M. J. L. Morales, A. G. Armada, and A. Burr, "BLER-SNR curves for 5G NR mcs under AWGN channel with optimum quantization," in *2024 IEEE 100th Vehicular Technology Conference (VTC2024-Fall)*. IEEE, 2024, pp. 1–6.

[29] D. A. Basnayaka, P. J. Smith, and P. A. Martin, "Performance analysis of macrodiversity MIMO systems with MMSE and ZF receivers in flat rayleigh fading," *IEEE transactions on wireless communications*, vol. 12, no. 5, pp. 2240–2251, 2013.

[30] A. Larranaga, S. Lagen, J. M. Fabrega, J. M. Rivas-Moscoso, J. P. Fernandez-Palacios, I. Tomkos, and R. Munoz, "Fronthaul/midhaul networks: Capacity and latency requirements imposed by 6g disaggregated rans," *IEEE Communications Magazine*, 2025.

[31] M. Rahmani, J. Zhao, V. Ranjbar, A. A. J. Al-Tahmeesschi, H. Ahmadi, A. G. Burr, and S. Pollin, "Exploring O-RAN compression techniques in decentralized distributed MIMO systems: Reducing fronthaul load," in *IEEE PIMRC*, 2025.

[32] B. Li, H. Zeng, X. Zhu, Y. Jiang, and Y. Wang, "Cooperative time synchronization and robust clock parameters estimation for time-sensitive cell-free massive MIMO systems," *IEEE Transactions on Wireless Communications*, 2024.

[33] Y. Feng, W. Zhang, Y. Ge, and H. Lin, "Frequency synchronization in distributed antenna systems: Pairing-based multi-CFO estimation, theoretical analysis, and optimal pairing scheme," *IEEE Transactions on Communications*, vol. 67, no. 4, pp. 2924–2938, 2018.

Mostafa Rahmani Ghourtani received his B.Sc. degree in Electrical Engineering from Shiraz University, Iran, in 2009, followed by an M.Sc. degree in Communication Systems Engineering from Tarbiat Modares University, Tehran, Iran, in 2012. He completed his Ph.D. in Communication Systems Engineering at Shiraz University of Technology, Iran, in 2023. Currently, he is a postdoctoral researcher at the University of York. His research interests focus on wireless communication systems, including MIMO and cell-free massive MIMO, Open RAN, physical layer network coding, and the application of machine learning and deep reinforcement learning in communications.

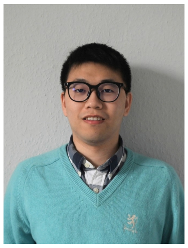

Junbo Zhao received the B.Eng. degree in Electronic Information Engineering from the Beijing Information Science and Technology University, Beijing, China in 2016, and the M.Sc. degree in Communications Engineering and Ph.D. degree in Electronic Engineering from the University of York, U.K. in 2019 and 2023, respectively. He is currently a post-doctoral researcher in the School of Physics, Engineering and Technology, University of York, U.K. His research interests include MIMO and Cell-free massive MIMO, optimal pilot assignment, channel estimation, physical layer data detection and quantization, and Open RAN.

Yi Chu received the B.Sc. degree in electronic engineering from China Agriculture University, Beijing, China, in 2008, and the M.Sc. degree in communications engineering and the Ph.D. degree in electronic engineering from the University of York, in 2009 and 2014, respectively. He was a Research Associate with the Center for High Altitude Platform Applications (CHAPA), University of York. He is currently a Research Fellow with the Institute for Safe Autonomy (ISA), School of Physics, Engineering and Technology, University of York. His research interests include wireless and quantum communications applications on aerial platforms, private 5G network deployments, open-RAN network implementation, communications system evaluation using software-defined radio, multi-element antenna array, wireless signal propagation, physical layer network coding, and intelligent medium access control for wireless sensor networks.

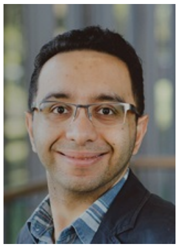

Hamed Ahmadi (Senior Member, IEEE) received the Ph.D. degree from the National University of Singapore in 2012. He is a Reader of Digital Engineering with the School of Physics, Engineering and Technology, University of York, U.K., where he is the Director of iTWINS Lab and the Deputy Pillar Lead for Advanced Communications with the Institute for Safe Autonomy. He is also an Adjunct Academic with the school of Electrical and Electronic Engineering, University College Dublin, Ireland. He was a SINGA Ph.D. Scholar with the Institute for Infocomm Research, A-STAR, National University of Singapore. Since, then he worked at different academic and industrial positions in the Republic of Ireland and U.K. He has published a book and more than 100 peer reviewed book chapters, journal, and conference papers. He is the ML/AI work package lead for the York-led YO-RAN and REACH, which are projects developing 6G open radio access networks in collaboration with industry and funded by U.K. Government. He has been the Networks Working Group Chair of COST Actions CA15104 (IRACON) and CA20120 (INTERACT). His current research interests include the application of machine learning in wireless networks, open radio access and networking, green and sustainable networks, airborne networks, digital twins of networks, and Internet-of-Things. He is an Associate Editorin-Chief of IEEE Communication Standards Magazine and a Fellow of U.K. Higher Education Academy. He had chairing roles in organising and technical programme committee of several IEEE flagship conferences, including IEEE ICC 2024, EUCNC 2025 and 2019, and PIMRC 2024 and 2019. He is also the Treasurer of the IEEE U.K. and Ireland Diversity, Equity, and Inclusion Committee.

David Grace (S'95-A'99-M'00-SM'13) received his PhD from University of York in 1999. He is now Professor (Research) and leads the Challenging Environments Research Theme in the School of Physics, Engineering and Technology, and is pillar lead for Advanced Communications in the university's Institute for Safe Autonomy, and Director of the Centre for High Altitude Platform Applications. Current research interests include resilient wireless systems, 5G/6G O-RAN systems, application of artificial intelligence to wireless communications, dynamic spectrum access and interference management. He led the recently completed £5.5M REACH and is a work package lead for the York-led £9.3M YO-RAN, which are projects developing 5G open radio access networks in collaboration with industry and funded by UK Government. He is an author of over 300 papers, and author/editor of 2 books. He is a member of UK Telecom Infrastructure Network's Expert Working Group on Non-Terrestrial Networks, which influences government policy and brings together disparate strands of expertise. He is the former chair of IEEE Technical Committee on Cognitive Networks in 2013/4 and a founding member of the IEEE Technical Committee on Green Communications and Computing. From 2014-8 he was a non-executive director of Stratospheric Platforms Ltd, which is developing high altitude platform based wireless systems.

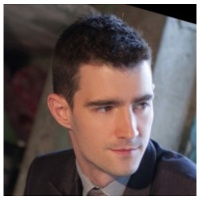

Robert G. Maunder (CEng, FIET, SMIEEE, SFHEA) is the founder and CTO of AccelerComm Ltd, which he spun-out of the University of Southampton, UK in 2016. Rob has studied with the School of Electronics and Computer Science at the University of Southampton, since October 2000. He was awarded a first class honours BEng in Electronic Engineering in July 2003, as well as a PhD in Telecommunications in December 2007. He began a lectureship in November 2007 and was promoted to Associate Professor in March 2013 and to Professor in August 2017. He was awarded Senior Member status of the IEEE in December 2012, Chartered Engineer status of the IET in November 2013 and Fellow status of the IET in January 2017. Rob's research interests include joint source/channel coding and the holistic design of algorithms and hardware implementations for wireless communications. He has published over 100 IEEE papers in these areas

Alister Burr (MIET, MIEEE, CEng) was born in London, U.K, in 1957. He received the BSc degree in Electronic Engineering from the University of Southampton, U.K in 1979 and the PhD from the University of Bristol in 1984. Between 1975 and 1985 he worked at Thorn-EMI Central Research Laboratories in London. In 1985 he joined the Department of Electronics (now part of the School of Physics, Engineering and Technology) at the University of York, U.K, where he has been Professor of Communications since 2000. His research interests are in wireless communication systems, including MIMO and cell-free massive MIMO, Open RAN, physical layer network coding, and iterative detection and decoding techniques. He has published more than 300 papers in refereed international conferences and journals, and is the author of "Modulation and Coding for Wireless Communications" (published by Prentice-Hall/PHEI), and co-author of "Wireless Physical-Layer Network Coding" (Cambridge University Press, 2018). In 1999 he was awarded a Senior Research Fellowship by the U.K. Royal Society, and in 2002 he received the J. Langham Thompson Premium from the Institution of Electrical Engineers. He has also given more than 20 invited presentations, including six keynote presentations. He has been co-chair, working group 2, of a series of European COST programmes including currently CA20120 INTERACT, and has also served as Associate Editor for IEEE Communications Letters, Workshops Chair for IEEE ICC 2016, and TPC co-chair for PIMRC 2018 and 2020.